J. Fluid Mech. (2026), *vol.* 1041, A39, doi:10.1017/jfm.2026.11966

Nonlinear surface gravity waves on a shear layer

Josh Shelton[1], **David Gerard Dritschel**[1] and **Wooyoung Choi**[2]

[1]School of Mathematics and Statistics, University of St Andrews, St Andrews KY16 9SS, UK

[2]Department of Mathematical Sciences, New Jersey Institute of Technology, Newark, NJ 07102-1982, USA

Corresponding author: Josh Shelton, josh.shelton@st-andrews.ac.uk

(Received 16 February 2026 UTC; revised 17 May 2026 UTC; accepted 6 July 2026 UTC)

We study large-amplitude travelling gravity waves on the free surface of an infinitely deep fluid with a shear layer of constant vorticity extending to a finite depth. A boundary-integral formulation is developed by using conformal mapping to describe the two free boundaries of the problem and is solved numerically using a pseudospectral method. The linear wavespeed c satisfies a cubic dispersion relation, which essentially arises from the combination of two gravity modes and a shear mode. For certain ranges of parameters, the collision of these modes leads to linear instability. The nonlinear solutions corresponding to one of the three values of c were studied by Milinazzo & Saffman (1990 *J. Fluid Mech.* 216, 93–101). These solutions are dominated by the surface gravity mode; however, the solutions associated with the remaining two values of c were overlooked. We study these new solutions in detail and find distinct properties from those calculated by Milinazzo & Saffman, such as the emergence of large-amplitude waves on the vorticity interface and changes in the relative phase between the two free boundaries. Moreover, bifurcations between shear and gravity modes are shown to emerge between solution branches of disparate wavenumbers under resonance conditions, which results in significant qualitative changes in the solution profiles across very small regions of parameter space.

Key words: waves/free-surface flows, shear waves, surface gravity waves

1. Introduction

When wind blows over an air–water interface, the resultant shear stress at the water surface induces a shear flow and its instability is one of main mechanisms for surface

© The Author(s), 2026. Published by Cambridge University Press. This is an Open Access article, distributed under the terms of the Creative Commons Attribution licence (https://creativecommons.org/licenses/by/4.0/), which permits unrestricted re-use, distribution and reproduction, provided the original article is properly cited.

https://doi.org/10.1017/jfm.2026.11966

wave generation in the ocean (Miles 1957; Sullivan & McWilliams 2010). The vorticity in the shear flow is typically concentrated near the water surface and decays with depth.

In this paper, we study the simplest possible model of this situation, consisting of two layers of different vorticity in an inviscid fluid of constant density. The lower fluid layer of infinite depth is irrotational while the upper fluid layer has constant, uniform, vorticity. Mathematically, this leads to a nonlinear problem with two free boundaries: one is the internal interface at the vorticity jump, and the other is the free surface of constant pressure at the top of the shear layer.

The linear dispersion relation for a free-surface fluid with an internal vorticity jump was studied by Stern & Adam (1973) and Caponp *et al.* (1991), who both obtained a cubic equation for the wavespeed and observed that at certain parameter values this base state is unstable when two out of the three wavespeeds become identical. Weakly nonlinear corrections to the linear wavespeed were obtained by Brevik (1978) by developing a Stokes expansion to third order, but the instability of the basic state and resonances between shear and gravity modes were not noticed. Fully nonlinear travelling-wave solutions were obtained numerically by Milinazzo & Saffman (1990) using a boundary-integral method. The nonlinear solutions obtained by Milinazzo & Saffman (1990) are characterised by a relatively large-amplitude surface displacement compared with that on the internal vorticity jump. However, out of the three possible solution branches that emerge from the cubic linear dispersion relation for the wavespeed, only the gravity-wave mode travelling in the direction of the shear flow was computed at finite amplitude in order to compare with the results of Banner & Phillips (1974) for the dependence of the maximum wave amplitude on the surface drift. Nonlinear solutions corresponding to the remaining two solutions of the cubic linear dispersion relation were neglected entirely.

The aim of the present paper is to study the nonlinear solutions associated with the two remaining solutions of the cubic linear dispersion relation. These new solutions display behaviour previously unseen, namely relatively large-amplitude waves at the vorticity jump and bifurcations between solutions branches with different wavenumbers. Each bifurcation occurs across a very small region of parameter space, and results in significant changes in the solution profiles – including a reversal of the dominant-amplitude interface, and a change in the polarity (measuring the alignment of the two wave crests).

A time-dependent conformal mapping is developed to study the nonlinear travelling-wave solutions that emerge in our model formulation. Similar conformal mappings have been used by Dyachenko *et al.* (1996) and Choi & Camassa (1999) for a free-surface fluid of finite depth, Choi (2009) and Murashige & Choi (2020) for a fluid layer of constant vorticity, Murashige & Choi (2022) for the interface between two fluid layers and Blyth & Părău (2016) for a fluid bounded both above and below by interfaces. The domain used in each of these approaches is analogous to both our irrotational fluid layer, bounded by a single interface, and to our shear layer of constant vorticity, bounded both above and below by interfaces. However, combining these two approaches to develop a conformal mapping appropriate to our model formulation raises an additional complication regarding continuity of solutions at the vorticity jump. This is resolved by creating an additional unknown at the internal interface to match each conformal domain together (see Murashige & Choi 2022, for an analogous approach). The principal advantage of the time-dependent conformal mapping over other steady boundary-integral approaches used by e.g. Milinazzo & Saffman (1990) is their time-dependent generalisation to study both stability and time evolution in general.

The paper is organised as follows. In § 2 we formulate the governing boundary-value problem for the nonlinear shear layer. The linear dispersion relation for the wavespeed is derived and some of the associated solutions are illustrated. The conformal mapping is

https://doi.org/10.1017/jfm.2026.11966

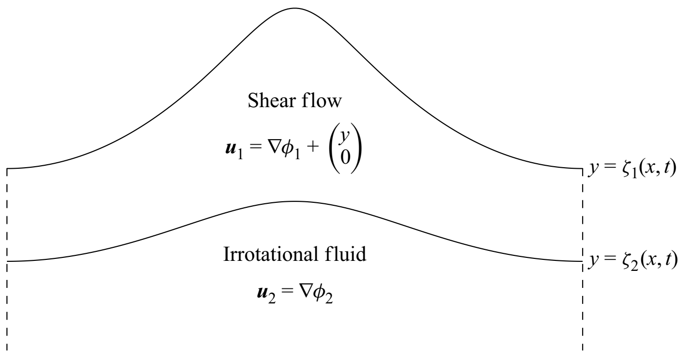

Figure 1. The domain $-\infty < y \leqslant \zeta_1(x, t)$ of the irrotational fluid, and the domain $-\zeta_1(x, t) \leqslant y \leqslant \zeta_2(x, t)$ of the rotational fluid is depicted. The vorticity of the upper fluid layer is constant, and there we employ the Helmholtz decomposition of the velocity field into an irrotational (potential) part and a linear horizontal shear flow. The shear flow is of unit strength due to the non-dimensionalisation used. Periodicity in x is assumed across the vertical dashed lines.

developed in § 3; here, we provide the final boundary-integral formulation in § 3.4 and details of the numerical method in § 3.5. Nonlinear solutions and their properties are then described in § 4. A discussion of our results and our conclusions are offered in § 5.

2. Mathematical formulation

We now present the non-dimensional boundary-value problem for the evolution of of a layer of constant vorticity lying below a free surface and above an irrotational fluid layer of infinite depth. Throughout this work we refer to the upper interface as the free surface and refer to the lower interface as the vorticity interface. The free surface is located at $y = \zeta_1(x, t)$, and the vorticity jump is located at $y = \zeta_2(x, t)$. We consider a two-dimensional flow with y pointing upwards and x horizontally. We nondimensionalise with respect to the shear strength ω and constant of gravitational acceleration g by taking g/ω^2 as a length scale and $1/\omega$ as a time scale. The irrotational fluid is located in the range $-\infty < y \leqslant \zeta_2(x, t)$, and the rotational fluid (the shear layer) is located within $\zeta_2(x, t) \leqslant y \leqslant \zeta_1(x, t)$. In denoting the (hereafter) non-dimensional velocity field in the upper layer by $\boldsymbol{u}_1 = (u_1, v_1)$ and that in the lower layer by $\boldsymbol{u}_2 = (u_2, v_2)$, we decompose $\boldsymbol{u}_1 = \boldsymbol{\nabla}\phi_1 + (y, 0)$ and $\boldsymbol{u}_2 = \boldsymbol{\nabla}\phi_2$, where $\phi_1(x, y, t)$ and $\phi_2(x, y, t)$ are the velocity potentials in each layer. The fluid domain and velocity field decomposition is depicted in figure 1.

A derivation of the following boundary-value problem from the dimensional Euler equations is provided in Appendix A. First, the velocity potential in each layer satisfies Laplace's equation

$$\nabla^2\phi_1 = 0 \quad \text{for} \quad \zeta_2(x, t) \leqslant y \leqslant \zeta_1(x, t), \tag{2.1a}$$

$$\nabla^2\phi_2 = 0 \quad \text{for} \quad -\infty < y \leqslant \zeta_2(x, t). \tag{2.1b}$$

At the free surface, $y = \zeta_1(x, t)$, there are both kinematic and dynamic boundary conditions given by

$$\zeta_{1t} = \phi_{1y} - \zeta_{1x}(\phi_{1x} + y) \quad \text{at} \quad y = \zeta_1(x, t), \tag{2.1c}$$

$$\phi_{1t} + \frac{1}{2}(\phi_{1x}^2 + \phi_{1y}^2) + y(\phi_{1x} + 1) - \psi_1 = B_1 \quad \text{at} \quad y = \zeta_1(x, t), \tag{2.1d}$$

https://doi.org/10.1017/jfm.2026.11966

respectively. The function $\psi_1(x, y, t)$ is the harmonic conjugate of $\phi_1(x, y, t)$, and B_1 is the Bernoulli constant. The boundary conditions holding at the vorticity interface $y = \zeta_2(x, t)$ are the kinematic condition and continuity of velocity, given by

$$\zeta_{2t} = \phi_{2y} - \zeta_{2x}\phi_{2x} \quad \text{at} \quad y = \zeta_2(x, t), \tag{2.1e}$$

$$\phi_{1x} + y = \phi_{2x}, \quad \phi_{1y} = \phi_{2y} \quad \text{at} \quad y = \zeta_2(x, t). \tag{2.1f}$$

Note that the shear flow in the upper fluid layer gives rise to all terms involving y in (2.1c) and (2.1f), as well as the terms $y\phi_{1x}$ and ψ_1 in (2.1d).

Lastly, we have far-field decay conditions on the velocity potential ϕ_2 and its harmonic conjugate ψ_2 given by

$$(\phi_2, \psi_2) \to (0, 0) \quad \text{as} \quad y \to -\infty. \tag{2.1g}$$

To summarise, the boundary-value problem (2.1) involves the unknown solutions ζ_1, ζ_2, ϕ_1 and ϕ_2, together with the Bernoulli constant B_1. By fixing the total volume of fluid in each layer, we obtain from Appendix A.2.1 the constraints

$$\frac{1}{L}\int_{-L/2}^{L/2} \zeta_1 \, \mathrm{d}x = H \quad \text{and} \quad \int_{-L/2}^{L/2} \zeta_2 \, \mathrm{d}x = 0, \tag{2.2}$$

where the (non-dimensional) parameters L and H are given by

$$L = \frac{\lambda\omega^2}{g} \quad \text{and} \quad H = \frac{h\omega^2}{g}. \tag{2.3}$$

Here, λ is the wavelength, ω is the shear strength, g is the constant acceleration of gravity and h is the mean depth of the shear layer. Thus, L is the non-dimensional wavelength and H is the non-dimensional mean shear-layer depth. Note that the limit of $g \to 0$ in which gravity is absent results in $L \to \infty$ and $H \to \infty$. Further, there are two distinguished limits in which the shear layer is removed: as $h \to 0$ we have $H \to 0$, and as $\omega \to 0$ we have both $L \to 0$ and $H \to 0$.

When solving for small-amplitude solutions in § 2.1, the resultant (possibly complex-valued) wavespeed c is a function of L and H. When solving for nonlinear travelling waves of permanent form, the real-valued c in this case depends additionally on a measure of the amplitude of the solution, detailed below. In both cases, c is the unknown of the problem.

2.1. *The linear dispersion relation*

We now study the behaviour and dispersion relation of small-amplitude solutions. When the amplitudes of both the free surface and vorticity interface are zero, an exact solution is known to the boundary-value problem (2.1), given by $\zeta_1 = H$, $\zeta_2 = 0$ and $\phi_1 = \phi_2 = \psi_1 = \psi_2 = 0$. Thus, in the study of small-amplitude solutions we consider

$$\zeta_1 \sim H + \epsilon\bar{\zeta}_1, \quad \zeta_2 \sim \epsilon\bar{\zeta}_2, \quad \phi_1 \sim \epsilon\bar{\phi}_1, \quad \phi_2 \sim \epsilon\bar{\phi}_2, \quad \psi_1 \sim \epsilon\bar{\psi}_1, \quad \psi_2 \sim \epsilon\bar{\psi}_2, \tag{2.4}$$

which hold as $\epsilon \to 0$. Further, the Bernoulli constant is expanded as $B_1 \sim H + \epsilon\bar{B}_1$. In order to solve for the perturbation quantities in (2.4) above, we first have to obtain the governing equations at $O(\epsilon)$. Note that the boundary conditions are evaluated at $y = \zeta_1(x, t)$ and $y = \zeta_2(x, t)$, which are also expanded in ϵ; these conditions are resolved by Taylor expanding each term.

The equations obtained at $O(\epsilon)$ are $\nabla^2\bar{\phi}_1 = 0$ for $0 \leqslant y \leqslant H$, and $\nabla^2\bar{\phi}_2 = 0$ for $-\infty < y \leqslant 0$. The far-field conditions are $(\bar{\phi}_2, \bar{\psi}_2) \to (0, 0)$ as $y \to -\infty$. The boundary conditions holding at $y = 0$ are $\bar{\zeta}_{2t} = \bar{\phi}_{2y}$, $\bar{\phi}_{2y} = \bar{\phi}_{1y}$, $\bar{\phi}_{2x} = \bar{\phi}_{1x} + \bar{\zeta}_2$ and $\bar{\psi}_2 = \bar{\psi}_1$. Those

https://doi.org/10.1017/jfm.2026.11966

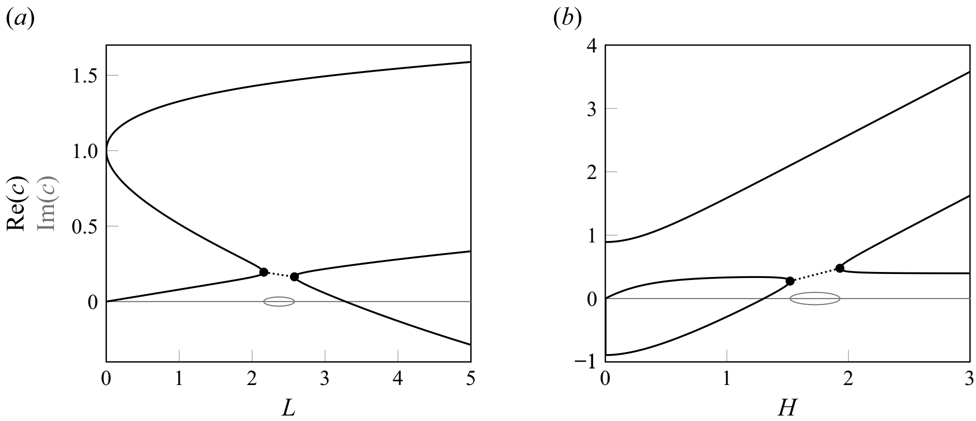

Figure 2. Solutions to the cubic linear dispersion relation (2.7) are shown for $H = 1$ in (*a*), and for $L = 5$ in (*b*). Values of Re[c] are shown in black and values for Im[c] in grey. In each figure there is a range of parameters for which unstable perturbations exist with Im[c] > 0, and the real parts of the wavespeed in these cases are shown with dotted lines. This occurs when two solutions of the cubic have the same real part and are complex conjugates of one another. The points of marginal stability are indicated with circles, and these are studied further across the parameter space in figure 3.

holding at $y = H$ are $\bar{\zeta}_{1t} = \bar{\phi}_{1y} - H\bar{\zeta}_{1x}$ and $\bar{\phi}_{1t} + H\bar{\phi}_{1x} - \bar{\psi}_1 + \bar{\zeta}_1 = \bar{B}_1$. The solutions to these can be written as

$$\{\bar{\zeta}_1, \bar{\zeta}_2\} = \{\alpha, \beta\}\mathrm{e}^{ik(x-ct)} + \text{c.c.}, \tag{2.5a}$$

$$\{\bar{\phi}_1, \bar{\psi}_1\} = \left[\{\mu, \mathrm{i}\mu\}\mathrm{e}^{ky} + \{\nu, -\mathrm{i}\nu\}\mathrm{e}^{-ky}\right]\mathrm{e}^{ik(x-ct)} + \text{c.c.}, \tag{2.5b}$$

$$\{\bar{\phi}_2, \bar{\psi}_2\} = \{\gamma, \mathrm{i}\gamma\}\mathrm{e}^{ik(x-ct)}\mathrm{e}^{ky} + \text{c.c.}, \tag{2.5c}$$

where c.c. denotes complex conjugate and $k = 2\pi n/L$ is the wavenumber (n is a positive integer). The solutions in (2.5*b*) and (2.5*c*) satisfy Laplace's equation, the Cauchy–Riemann equations applied to the analytic functions $\bar{\phi}_1 + \mathrm{i}\bar{\psi}_1$ and $\bar{\phi}_2 + \mathrm{i}\bar{\psi}_2$, as well as the decay conditions $(\bar{\phi}_2, \bar{\psi}_2) \to (0, 0)$. In (2.5), $c \in \mathbb{C}$ is the complex-valued unknown whose real and imaginary parts are the speed and growth rate of the perturbations, respectively.

Substituting solutions (2.5) into the $O(\epsilon)$ equations yields the algebraic equations

$$\begin{aligned}
&\gamma = \mu - \nu, \qquad \mathrm{i}k\gamma = \beta + \mathrm{i}k(\mu + \nu), \qquad \gamma = -\mathrm{i}c\beta, \\
&\mathrm{i}(H - c)\alpha = \mu\mathrm{e}^{kH} - \nu\mathrm{e}^{-kH} \qquad \text{and} \\
&\mathrm{i}k(H - c)[\mu\mathrm{e}^{kH} + \nu\mathrm{e}^{-kH}] - \mathrm{i}[\mu\mathrm{e}^{kH} - \nu\mathrm{e}^{-kH}] + \alpha = 0.
\end{aligned} \tag{2.6}$$

In solving this set of five equations for the five unknown constants, non-trivial solutions exist only when the dispersion relation

$$(H - c + 1)\left(2kc - 1 + \mathrm{e}^{-2kH}\right) = k(H - c)^2\left(2kc - 1 - \mathrm{e}^{-2kH}\right) \tag{2.7}$$

is satisfied. This is a cubic equation for the unknown c, in terms of H and $k = 2\pi n/L$. The real part, Re[c], corresponds to the wavespeed of time-dependent perturbations to the flat wave state, and the imaginary part, Im[c], to the growth rate of the perturbations.

Solutions of the cubic dispersion relation (2.7) are shown in figure 2 for $n = 1$, firstly for $H = 1$ in figure 2(*a*) and for $L = 5$ in figure 2(*b*). In each case, we see that there is a range of the remaining parameter (L or H) for which the time-dependent perturbation is

https://doi.org/10.1017/jfm.2026.11966

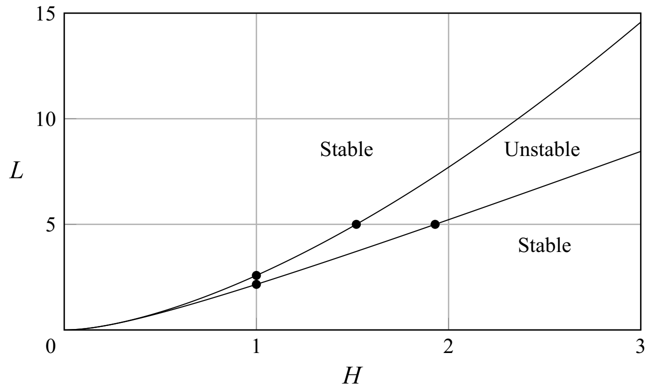

Figure 3. Values of H and L for which small-amplitude perturbations to the base state, $\zeta_1(x,t)=H$ and $\zeta_2(x,t)=0$, are marginally stable are shown. This corresponds to two repeated real-valued roots to the cubic dispersion relation (2.7) for c. We have taken $n=1$ which results in one wave period within the periodic domain. Black curves show the edge of the marginally stable parameter region, within which the linear solutions are unstable. Black circles correspond to the four locations of marginal stability seen in figure 2. This figure is comparable to figure 1 from Caponp *et al.* (1991).

unstable. For instance, in figure 2(a), which has $H=1$, there are three marginally stable modes (solutions with $\mathrm{Im}[c]=0$) for $0\leqslant L\leqslant 2.1589$ and $L\geqslant 2.5814$. When $2.1589<L<2.5814$, there is one marginally stable mode and two complex-conjugate modes with $\mathrm{Im}[c]\neq 0$; these correspond to stable and unstable modes with the same value of the wavespeed, $\mathrm{Re}[c]$.

The values of H and L that correspond to the edge of the region of instability may be determined by further studying the cubic dispersion relation (2.7). At the edge of the instability region, the complex-conjugate roots have $\mathrm{Im}[c]=0$ and therefore are repeated roots. In writing this dispersion relation in the form $c^3+a_2c^2+a_1c+a_0=0$, where a_0, a_1 and a_2 are known functions of L and H, we identify a repeated root by factorising the cubic as $(c-\alpha)^2(c-\beta)=0$, where $c=\alpha$ is the repeated root. Equating these two representations of the cubic dispersion relation yields three constraints for the two unknowns α and β. Two of these constraints determine $\alpha=-a(a_2+\sqrt{a_2^2-3a_1})/3$ and $\beta=-a_2-2\alpha$, and the remaining constraint requires $\alpha^2(a_2+2\alpha)-a_0=0$, which forms an implicit relation for L and H. We solve this constraint numerically by Newton iteration, the results of which are shown in figure 3 with $n=1$. Two branches of parameter values exist as shown in this figure. For every value of H, there exists a range of values of L for which the time-dependent perturbation of the base state is unstable.

We can also study the three solutions of dispersion relation (2.7) under the limits of $k\to 0$ and $k\to\infty$. Firstly, for the long-wave limit of $k\to 0$ we obtain

$$c\sim H-H^2k \quad \text{and} \quad c\sim \pm k^{-1/2}+\frac{H^2}{2}k, \tag{2.8a}$$

and for short waves with $k\to\infty$ we obtain

$$c\sim \frac{1}{2}k^{-1} \quad \text{and} \quad c\sim H\pm k^{-1/2}. \tag{2.8b}$$

In each case, the two latter modes correspond to gravity waves on infinite depth in the presence of a mean current.

https://doi.org/10.1017/jfm.2026.11966

2.2. *Travelling-wave solutions of small amplitude*

When the wavespeed c is real valued, the small-amplitude disturbances studied in § 2.1 are travelling waves. The corresponding solutions for each interface are then given by

$$\zeta_1(x,t) \sim H + A\cos\big(k(x-ct)\big), \tag{2.9a}$$

$$\zeta_2(x,t) \sim -\frac{2k(H-c)\mathrm{e}^{-kH}}{(2kc-1)+\mathrm{e}^{-2kH}} A\cos\big(k(x-ct)\big), \tag{2.9b}$$

where $0 \leqslant A \ll 1$, and $k = 2\pi n/L$. We have considered the case for which A is non-negative without any loss of generality – the case with negative A is captured automatically due to translational invariance. Recall that $\zeta_1(x,t)$ is the free surface that bounds the rotational fluid with a region of uniform pressure, and $\zeta_2(x,t)$ is the vorticity interface between the two fluids. Two interesting cases emerge in the linear solutions (2.9). Firstly, if $c = c_1 = (1-\mathrm{e}^{-2kH})/(2k)$, then the solution for $\zeta_1(x,t)$ in (2.9*a*) is constant, $\zeta_1 = H$. This corresponds to a travelling wave on the vorticity interface when the top free surface is replaced by a rigid boundary, which was studied by Rayleigh (1894). Therefore, $c = c_1$ represents the linear speed of the shear wave mode. Secondly, if $c = c_2 = H$, then the solution for $\zeta_2(x,t)$ in (2.9*b*) is identically zero. This corresponds to a linear surface wave and a zero-amplitude vorticity interface.

Notice that the solutions with $c_1 = (1-\mathrm{e}^{-2kH})/(2k)$ and $c_2 = H$ are obtained as possible solutions from the linear dispersion (2.7) relation only in the limits of $H \to \infty$ and $H \to 0$ with $k \to \infty$ such that kH is finite. These values of c are shown in the (c, H) plane in figure 4 for $n = 1$ and $L = 5$, where the solid lines are solutions of the dispersion relation with $\mathrm{Im}[c] = 0$. Here, the values of c_1 are indicated by the dotted line and those of c_2 by the dashed line. By expanding the dispersion relation as $H \to \infty$, the two solution branches parallel to $c_2 = H$ as $H \to \infty$ in figure 4 may be obtained as $c \sim H - 1/(2k) \pm \sqrt{(1+4k)/(4k^2)} + O(H^{-1})$, and therefore represent two gravity modes on an infinite-depth fluid with constant vorticity.

As a measure of the solution amplitude, we employ the sum of individual amplitudes defined by

$$A = \frac{\max(\zeta_1) - \min(\zeta_1) + \max(\zeta_2) - \min(\zeta_2)}{L}, \tag{2.10}$$

which is positive definite and tends to zero in the small-amplitude limit of $\epsilon \to 0$ from (2.4). Note that there are many ways to define an amplitude condition for these solutions. For instance, in the study by Milinazzo & Saffman (1990), the condition $\max(\zeta_1) - \min(\zeta_1)$ was used, but this has the issue of permitting highly nonlinear vorticity interfaces with $\zeta_2 = O(1)$ in the limit of small amplitude. Alternative choices are the momentum and energy derived in Appendix A.2, which are conserved quantities of the time-dependent system. However, the value of these is finite and non-zero in the small-amplitude limit; moreover when shifted by a constant to ensure that the momentum and energy tend to zero in the small-amplitude limit, they fail to be positive definite.

Small-amplitude solutions are shown across each of the three solution branches in figure 4 for $L = 5$. These solutions were calculated with an amplitude of $A = 10^{-5}$ from (2.10). Along the solution branch with the largest value of the wavespeed c corresponding to the gravity-wave mode travelling in the same direction as the shear flow, the amplitude of the free surface $\zeta_1(x)$ is large and the amplitude of the vorticity interface $\zeta_2(x)$ is small. This is seen in profiles figure 4(*a–c*) here, as $H \to \infty$ along this branch we have $\zeta_2 \to 0$. The remaining two solution branches consist of solutions with a larger-amplitude vorticity interface. The branch starting from $c = 0$ corresponds to the shear wave mode while the

https://doi.org/10.1017/jfm.2026.11966

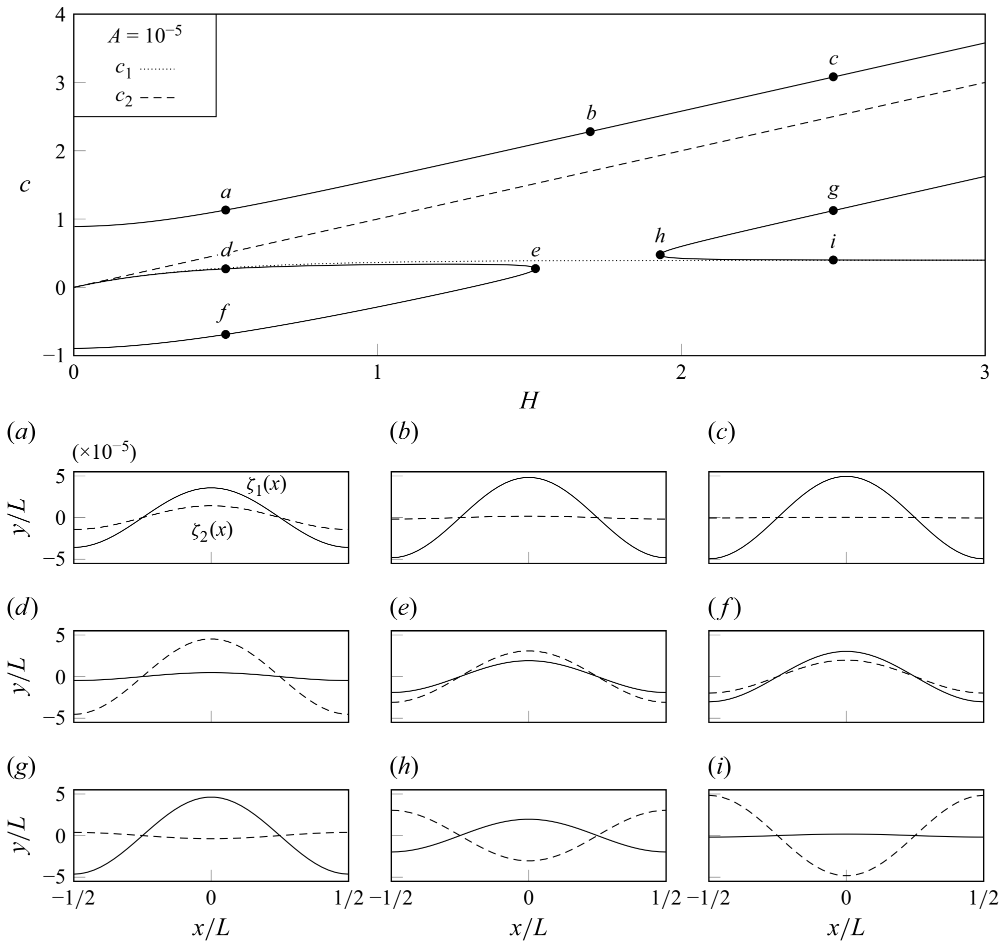

Figure 4. Branches of travelling-wave solutions are shown with solid lines in the (H, c) plane for fixed $L = 5$, $n = 1$ and $A = 10^{-5}$ from the amplitude condition (2.10). The condition $c_1 = (1 - e^{-2kH})/(2k)$ which results in $\zeta_1(x) = 0$ is shown dotted, and $c_2 = H$ which results in $\zeta_2(x) = 0$ is shown dashed. Panels (*a*) to (*i*) show the nine labelled solution profiles. In these, the free surface $\zeta_1(x)$ is shown in black, and the vorticity interface $\zeta_2(x)$ is shown dashed. Note that we have plotted $\zeta_1 - H$ in order to see the surface profile more clearly. The upper branch with the largest value of c corresponds to the solutions calculated by Milinazzo & Saffman (1990).

remaining branch represents the gravity-wave mode travelling in the opposite direction to the shear flow. These two modes collide as the value of H increases and subsequently lose their stability. Along the solution branch containing d, e and f, or before the collision occurs, the free surface and vorticity interface have the same polarity, whereas along branch g, h, i this polarity is opposite to one another. Along these two branches, we have that the $\zeta_1(x) \to 0$ as $H \to 0$ starting from solution d, and also as $H \to \infty$ starting from solution i. Further, on the third solution branch we have $\zeta_2(x) \to 0$ as $H \to \infty$ when starting from solution g.

All solutions shown in figure 4 have $n = 1$ (which enters into the wavenumber $k = 2\pi n/L$), and so have one wave period within the periodic domain. The linear dispersion relation (2.7) involves k, and so branches computed with different wavenumbers have different values of the wavespeed c. The linear branches of solutions with $n = 1$, $n = 2$ and $n = 3$ are shown in figure 5 for $L = 5$. We see that solution branches with different

https://doi.org/10.1017/jfm.2026.11966

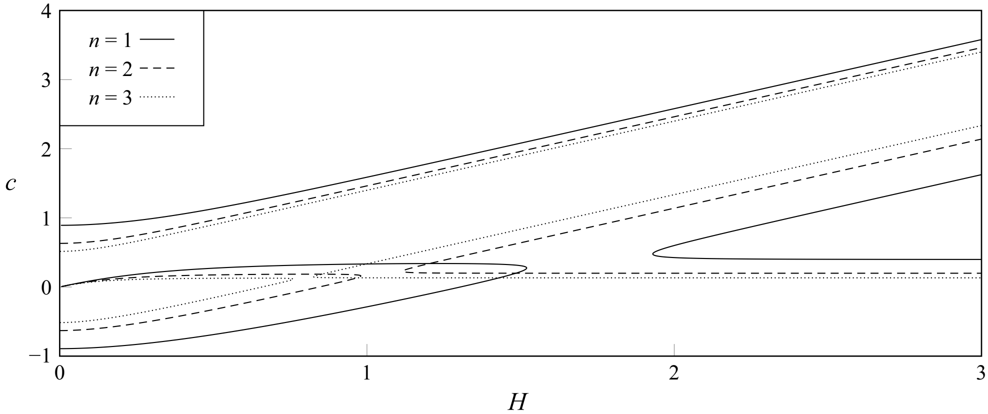

Figure 5. Branches of linear solutions are shown in the (H, c) plane for $L = 5$ and $A = 10^{-5}$. The three branches with $n = 1$ were shown in figure 4. Here, n represents the number of wave periods within the periodic domain. Also shown are the solution branches with $n = 2$ (dashed) and $n = 3$ (dotted). Solution branches with different wavenumbers intersect with one another, which leads to the bifurcations of nonlinear solutions studied in § 4.

wavenumbers intersect with one another at multiple places. This means that at certain parameter values, there exist linear modes with different wavenumbers that travel at the same speed. In general, if it exists, this so-called resonance between gravity and shear wave modes with wavenumbers $k_n = 2\pi n/L$ and $k_m = 2\pi m/L$ can occur at two wavespeeds determined from (2.7) by

$$\frac{\left(2k_n c - 1 + \mathrm{e}^{-2k_n H}\right)}{n\left(2k_n c - 1 - \mathrm{e}^{-2k_n H}\right)} = \frac{\left(2k_m c - 1 + \mathrm{e}^{-2k_m H}\right)}{m\left(2k_m c - 1 - \mathrm{e}^{-2k_m H}\right)}. \tag{2.11}$$

Analogous behaviour arises for gravity-capillary waves on infinite depth as first shown by Wilton (1915). A weakly-nonlinear theory was developed by Chen & Saffman (1979) to resolve this issue for gravity-capillary waves, and it was shown that when linear dispersion curves cross there emerge bifurcations between these, which was later confirmed in a numerical work by Chen & Saffman (1980). The same phenomenon emerges in our model formulation due to the crossing of linear solution branches. A numerical method to study this phenomenon for fully nonlinear solutions is now developed.

3. The boundary-integral formulation

In order to obtain numerical solutions to the nonlinear boundary-value problem (2.1), we employ a conformal map which takes the free surface $y = \zeta_1(x, t)$ and vorticity jump $y = \zeta_2(x, t)$ to a known location in the conformal domain. We first develop the time-dependent conformal mapping in § 3.1 to § 3.3, and then reduce this to the steady conformal mapping in § 3.4. The remainder of the paper focuses on computing travelling-wave solutions in a co-moving frame of speed c with the steady conformal mapping; however, the method is first developed for the fully time-dependent case so that time evolution and stability can be studied in subsequent works without changing the formulation.

3.1. *The time-dependent conformal mapping*

A different conformal map must be used for each of the two fluid layers. For the irrotational fluid confined within $-\infty < y \leqslant \zeta_2(x, t)$, we consider the map that takes (x, y) to (ξ_2, η_2),

https://doi.org/10.1017/jfm.2026.11966

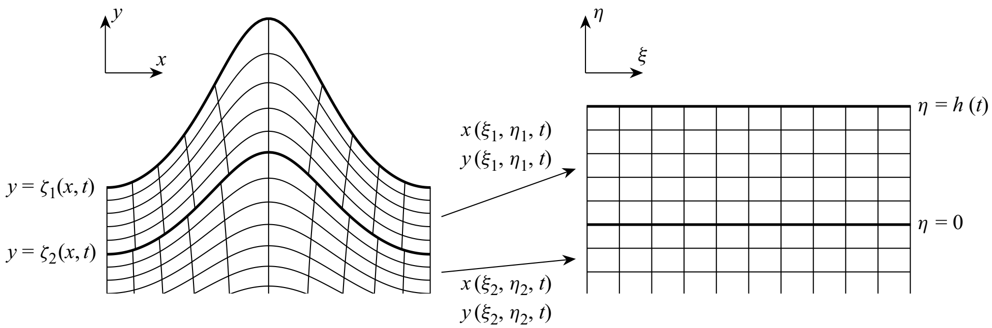

Figure 6. The time-dependent mapping from the physical (x, y) plane to the conformal (ξ, η) plane is shown. Each fluid region, $-\infty < y \leqslant \zeta_2$ and $\zeta_2 \leqslant y \leqslant \zeta_1$, involves a distinct conformal map. The function $\gamma(\xi, t)$ is introduced in § 3.2 to enforce continuity of physical quantities across each mapped region at $\eta = 0$.

such that the fluid is located in the range $-\infty < \eta_2 \leqslant 0$. For the rotational fluid located in the range $\zeta_2(x, t) \leqslant y \leqslant \zeta_1(x, t)$, we consider the map that takes (x, y) to (ξ_1, η_1), such that the fluid is located in the range $0 \leqslant \eta_1 \leqslant h(t)$. This mapping is depicted in figure 6. The conformal method developed in this section was originally derived for a single bounded fluid layer (Choi & Camassa 1999) and was extended to the case of two unbounded fluid layers by Murashige & Choi (2022). Our implementation requires the combination of an unbounded lower layer for the irrotational fluid, and a bounded upper region for the vorticity layer.

The solutions in the lower fluid layer are then given by $x_2(\xi_2, \eta_2, t)$, $y_2(\xi_2, \eta_2, t)$, $\phi_2(x_2(\xi_2, \eta_2, t), y_2(\xi_2, \eta_2, t), t)$ and $\psi_2(x_2(\xi_2, \eta_2, t), y_2(\xi_2, \eta_2, t), t)$. Each of these satisfies Laplace's equation within the conformal domain (i.e. $\nabla^2 y_2 = \partial^2_{\xi_2} y_2 + \partial^2_{\eta_2} y_2 = 0$). Further, we have the decay conditions $x_2 \sim \xi_2$, $y_2 \sim \eta_2$, $\phi_2 \to 0$ and $\psi_2 \to 0$ as $\eta_2 \to -\infty$, the first two of which are obtained from requirements of the map, and the latter two from (2.1*g*). Since the functions $x_2 + \mathrm{i}y_2$ and $\phi_2 + \mathrm{i}\psi_2$ are harmonic, it suffices to solve only for the imaginary part of each and then use the Cauchy–Riemann equations to obtain the solution for the real part. The solutions of these conformal boundary-value problems are then given by

$$\{x_2, y_2\} = \{\xi_2, \eta_2\} + \sum_{\substack{m=-\infty \\ m\neq 0}}^{\infty} \{-\mathrm{i} \cdot \mathrm{sgn}(m) a_m(t), a_m(t)\} \mathrm{e}^{|m|k\eta_2} \mathrm{e}^{imk\xi_2}, \tag{3.1a}$$

$$\{\phi_2, \psi_2\} = \sum_{\substack{m=-\infty \\ m\neq 0}}^{\infty} \{-\mathrm{i} \cdot \mathrm{sgn}(m) b_m(t), b_m(t)\} \mathrm{e}^{|m|k\eta_2} \mathrm{e}^{imk\xi_2}, \tag{3.1b}$$

where $\mathrm{sgn}(m)$ is the signum function and $k = 2\pi n/L$.

In the upper fluid layer, we denote the solutions by $x_1(\xi_1, \eta_1, t)$, $y_1(\xi_1, \eta_1, t)$, $\phi_1(x_1(\xi_1, \eta_1, t), y_1(\xi_1, \eta_1, t), t)$ and $\psi_1(x_1(\xi_1, \eta_1, t), y_1(\xi_1, \eta_1, t), t)$. These satisfy Laplace's equation for $0 \leqslant \eta_1 \leqslant h(t)$, as well as matching constraints with the solutions (3.1) of the lower fluid layer at $\eta_1 = 0$. A difficulty that arises with this matching is that the horizontal conformal coordinates are not equal at the vorticity interface $\eta_2 = 0$ and $\eta_1 = 0$, and require the introduction of an intermediary variable (which itself is an unknown of the problem). This process is detailed further in § 3.2. The solutions in the upper fluid layer

https://doi.org/10.1017/jfm.2026.11966

may be obtained as

$$y_1 = \eta_1 + c_0(t) + \sum_{\substack{m=-\infty \\ m\neq 0}}^{\infty} \left[c_m(t)\mathrm{e}^{mk\eta_1} + d_m(t)\mathrm{e}^{-mk\eta_1}\right]\mathrm{e}^{imk\xi_1}, \tag{3.2a}$$

$$\phi_1 = e_0(t)\xi_1 + f_0(t)\eta_1 + g_0(t) + \sum_{\substack{m=-\infty \\ m\neq 0}}^{\infty} \left[e_m(t)\mathrm{e}^{mk\eta_1} + f_m(t)\mathrm{e}^{-mk\eta_1}\right]\mathrm{e}^{imk\xi_1}. \tag{3.2b}$$

Solutions for x_1 and ψ_1 can be obtained by integrating the Cauchy–Riemann equations $x_{1\xi_1} = y_{1\eta_1}$ and $\psi_{1\xi_1} = -\phi_{1\eta_1}$, with the constant of integration for x_1 determined by the condition $x_1(0, 0, t) = 0$.

In this formulation, we restrict solutions (3.1) in the lower fluid layer to $\eta_2 = 0$, and (3.2) solutions in the upper fluid layer to both $\eta_1 = 0$ and $\eta_1 = h(t)$. The solutions on the boundaries are represented with capital letters, for instance those for the vertical coordinates y_1 and y_2 are

$$Y_{1U}(\xi_1, t) = y_1(\xi_1, h(t), t), \quad Y_{1L}(\xi_1, t) = y_1(\xi_1, 0, t), \quad Y_{2U}(\xi_2, t) = y_2(\xi_2, 0, t). \tag{3.3a}$$

The subscript number refers to the original fluid layer, while the subscript letter denotes whether the solution has been evaluated at the upper or lower surface that bounds the respective layer. For instance, Y_{1U} denotes the solution $y_1(\xi_1, \eta_1, t)$ evaluated at the upper interface $\eta_1 = h(t)$ of layer one. Equivalent definitions are also introduced for X_{1U}, X_{1L}, X_{2U}, Φ_{1U}, Φ_{1L}, Φ_{2U}, Ψ_{1U}, Ψ_{1L} and Ψ_{2U}.

The quantities for the lower fluid layer are related by the Hilbert transform (see below), giving

$$X_{2U} = \xi_2 - \mathscr{H}[Y_{2U}], \quad \Phi_{2U} = -\mathscr{H}[\Psi_{2U}]. \tag{3.4}$$

The harmonic relations (3.4) relate the real and imaginary parts of an analytic function that decays to zero as $\eta_2 \to -\infty$. Note that the relation $\Psi_{2U} = \mathscr{H}[\Phi_{2U}]$ is also required for the time-dependent mapping, in which an evolution equation is first obtained for Φ_{2U}. The operator $\mathscr{H}$ appearing in (3.4) is the Hilbert transform, defined by

$$\mathscr{H}[Y] = \frac{1}{\pi} \int_{-\infty}^{\infty} \frac{Y(\tilde{\xi})}{\tilde{\xi} - \xi} \mathrm{d}\tilde{\xi}. \tag{3.5}$$

Analogous harmonic relations are obtained for the quantities for the upper fluid layer, which are given by

$$X_{1L} = \xi_1 + \mathscr{T}[Y_{1L}] - \mathscr{S}[Y_{1U}], \quad X_{1U} = \xi_1 + \mathscr{S}[Y_{1L}] - \mathscr{T}[Y_{1U}], \tag{3.6}$$

$$\Phi'_{1L} = A_0 + \mathscr{T}[\Psi'_{1L}] - \mathscr{S}[\Psi'_{1U}], \quad \Phi'_{1U} = A_0 + \mathscr{S}[\Psi'_{1L}] - \mathscr{T}[\Psi'_{1U}], \tag{3.7}$$

where $A_0 = (Lh)^{-1} \int_{-L/2}^{L/2} [\Psi_{1U} - \Psi_{1L}] \mathrm{d}\xi_2$. The operators $\mathscr{T}$ and $\mathscr{S}$ are principal-valued integrals defined by

$$\mathscr{T}[Y] = \int_{-\infty}^{\infty} \frac{Y(\tilde{\xi})}{2h} \coth\left[\frac{\pi(\tilde{\xi} - \xi)}{2h}\right] \mathrm{d}\tilde{\xi}, \quad \mathscr{S}[Y] = \int_{-\infty}^{\infty} \frac{Y(\tilde{\xi})}{2h} \tanh\left[\frac{\pi(\tilde{\xi} - \xi)}{2h}\right] \mathrm{d}\tilde{\xi}, \tag{3.8}$$

where $h = L^{-1} \int_{-L/2}^{L/2} (Y_{1U} - Y_{1L}) \mathrm{d}\xi_1$. In practise, we calculate each of the three principal-valued integrals spectrally with the Fourier multipliers detailed in § 3.5.

https://doi.org/10.1017/jfm.2026.11966

By using the chain rule, expressions can be obtained for partial derivatives with respect to x and y in terms of the conformal coordinates ξ_1 and η_1, or ξ_2 and η_2. The Cauchy–Riemann equations are then used to eliminate derivatives with respect to η_1 and η_2. This results in expressions which only involve differentiation with respect to ξ_1 or ξ_2, which are used to convert the two-dimensional boundary-value problem (2.1) into a one-dimensional boundary-integral formulation. We use primes ($\prime$) to denote differentiation with respect to either ξ_1 or ξ_2, depending on the dependence of the function. For instance, Y'_{1U} denotes $\partial_{\xi_1} Y_{1U}$. We then obtain $\zeta_{1x} = Y'_{1U}/X'_{1U}$, $\zeta_{2x} = Y'_{1L}/X'_{1L}$ and $\zeta_{2x} = Y'_{2U}/X'_{2U}$ for the derivatives of each interface. Derivatives of the velocity potential are found to be $\phi_{1x} = (Y'_{1U}\Psi'_{1U} + X'_{1U}\Phi'_{1U})/J_{1U}$ and $\phi_{1y} = (Y'_{1U}\Phi'_{1U} - X'_{1U}\Psi'_{1U})/J_{1U}$, with equivalent results holding for ϕ_{1x}, ϕ_{1y}, ϕ_{2x} and ϕ_{2y} evaluated at the lower interface, $\eta_1 = \eta_2 = 0$. Here, we have defined $J_{1U}(\xi_1, t) = (X'_{1U})^2 + (Y'_{1U})^2$ and $J_{2L}(\xi_2, t) = (X'_{2L})^2 + (Y'_{2L})^2$, which are the Jacobians of each conformal map.

3.2. *Matching conditions at the vorticity interface*

At the vorticity interface $y = \zeta_2(x, t)$, which is specified in conformal coordinates by both $\eta_1 = 0$ and $\eta_2 = 0$, there are four matching conditions that must hold. These are $x_2 = x_1$, $y_2 = y_1$ and continuity of horizontal and vertical velocities across the interface. These latter two conditions are given by $\phi_{2x} = \phi_{1x} + y_1$ and $\phi_{2y} = \phi_{1y}$ from (2.1*f*). Only three of these have to be enforced on solutions of the system, from which the other conditions are automatically satisfied. These three conditions are

$$X_{2U}(\hat{\xi} + \gamma(\hat{\xi}, t), t) = X_{1L}(\hat{\xi} - \gamma(\hat{\xi}, t), t), \tag{3.9a}$$

$$Y_{2U}(\hat{\xi} + \gamma(\hat{\xi}, t), t) = Y_{1L}(\hat{\xi} - \gamma(\hat{\xi}, t), t), \tag{3.9b}$$

as well as continuity of the horizontal velocity, which when written in terms of the conformal solutions using the chain rule yields

$$\frac{Y'_{2U}\Psi'_{2U} + X'_{2U}\Phi'_{2U}}{J_{2U}} = \frac{Y'_{1L}\Psi'_{1L} + X'_{1L}\Phi'_{1L}}{J_{1L}} + Y_{1L}. \tag{3.9c}$$

In (3.9*c*) above, the left-hand side is evaluated at $\xi_2 = \hat{\xi} + \gamma(\hat{\xi}, t)$, and the right-hand side at $\xi_1 = \hat{\xi} - \gamma(\hat{\xi}, t)$. Primes ($\prime$) denote differentiation with respect to the conformal coordinate ξ_1 or ξ_2. Further, the unknown function $\gamma(\hat{\xi}, t)$, introduced from taking $\xi_1 = \hat{\xi} - \gamma(\hat{\xi}, t)$ and $\xi_2 = \hat{\xi} + \gamma(\hat{\xi}, t)$, satisfies $\gamma(\pm L/2, t) = 0$. An analogous method was used by Murashige & Choi (2022) to study the nonlinear interface problem between two immiscible fluids with different densities, following Saffman & Yuen (1982). Note that in formulations where neither the horizontal or vertical components of the velocity field are continuous across the interface, such as for a density jump, the normal component of the velocity field would be continuous, but the tangential component would be discontinuous.

3.3. *Conserved quantities*

There are four conserved quantities of our model formulation: mass of the upper rotational fluid layer, mass of the lower irrotational fluid layer, horizontal momentum and energy. Their conservation laws are derived in Appendix A.2 from solutions of the dimensional two-dimensional boundary-value problem, and in the same section are reduced to a one-dimensional form involving only quantities evaluated at each interface. We now express these in terms of the conformal coordinates, ξ_1 and ξ_2. Firstly, the mass conditions (2.2) are written in conformal coordinates by using the chain rule at the lower (internal) interface

https://doi.org/10.1017/jfm.2026.11966

to find $\mathrm{d}x = X'_{2U}\mathrm{d}\xi_2$, and at the upper free surface to find $\mathrm{d}x = X'_{1U}\mathrm{d}\xi_1$, where primes ($\prime$) denote partial derivatives with respect to the spatial variable. This yields

$$\frac{1}{L}\int_{-L/2}^{L/2} Y_{1U}X'_{1U}\mathrm{d}\xi_1 = H, \quad \int_{-L/2}^{L/2} Y_{2U}X'_{2U}\mathrm{d}\xi_2 = 0. \tag{3.10a,b}$$

Next, we consider the momentum P and energy E of the system given as boundary-integral expressions involving integration over x from (A8) and (A11). Upon non-dimensionalisation and writing in conformal coordinates, the expressions

$$P = \int_{-L/2}^{L/2}\left[-Y_{1U}\Psi'_{1U} + \frac{1}{2}(Y_{1U}^2X'_{1U} + Y_{1L}^2X'_{1L})\right]\mathrm{d}\xi_1, \tag{3.11a}$$

$$\begin{aligned} E = &\int_{-L/2}^{L/2}[(\Psi_{1U} + Y_{1U}^2)\Phi'_{1U} - (\Psi_{1L} + Y_{1L}^2)\Phi'_{1L}]\mathrm{d}\xi_1 + \int_{-L/2}^{L/2}\Psi_{2U}\Phi'_{2U}\,\mathrm{d}\xi_2 \\ &+ \int_{-L/2}^{L/2}\left[\frac{1}{3}(Y_{1U}^3X'_{1U} - Y_{1L}^3X'_{1L}) + \frac{1}{2}Y_{1U}^2X'_{1U}\right]\mathrm{d}\xi_1, \end{aligned} \tag{3.11b}$$

are obtained.

3.4. *The steady conformal mapping*

The remainder of this paper considers travelling-wave solutions of the time-independent formulation. We now study solutions that are steady in a frame of reference moving to the right with non-dimensional speed c. The Galilean transformation $x \mapsto x + ct$ results in $\phi_{1t} \mapsto \phi_{1t} - c\phi_{1x}$ and $\zeta_{1t} \mapsto \zeta_{1t} - c\zeta_{1x}$ in boundary conditions (2.1c) and (2.1d). Then, by setting ϕ_{1t} and ζ_{1t} to zero, we obtain solutions that are steady in the co-moving frame.

First, we convert the steady kinematic boundary conditions (2.1c) and (2.1e) at the free surface and vorticity interface into conformal coordinates, which yields

$$\Psi'_{1U} = (c - Y_{1U})Y'_{1U}, \quad \Psi'_{1L} = (c - Y_{1L})Y'_{1L}, \quad \Psi'_{2U} = cY'_{2U}. \tag{3.12}$$

These exact solutions may be integrated to obtain

$$\Psi_{1U} = C_1 + cY_{1U} - \frac{1}{2}Y_{1U}^2, \quad \Psi_{1L} = C_2 + cY_{1L} - \frac{1}{2}Y_{1L}^2, \quad \Psi_{2U} = C_3 + cY_{2U}, \tag{3.13}$$

where C_1, C_2 and C_3 are constants of integration. We have $C_2 = C_3$ from enforcing $\psi_2 = \psi_1 + y^2/2$ at the vorticity jump, and the solution $C_2 = C_3 = -cL^{-1}\int_{-L/2}^{L/2} Y_{2U}\mathrm{d}\xi_2$ is obtained from (3.1b). The constant C_1 is an unknown to be determined. Next, we consider the dynamic boundary condition at the free surface in (2.1d), which yields

$$\frac{(\Psi'_{1U})^2 + (\Phi'_{1U})^2}{2J_{1U}} + (Y_{1U} - c)\frac{Y'_{1U}\Psi'_{1U} + X'_{1U}\Phi'_{1U}}{J_{1U}} - \Psi_{1U} + \frac{Y_{1U}}{F^2} = B_1. \tag{3.14}$$

To summarise, the steady boundary-value problem involves the four unknown functions $Y_{1U}(\xi_1)$, $Y_{1L}(\xi_1)$, $Y_{2U}(\xi_2)$ and $\gamma(\hat{\xi})$, which are closed by the four equations (3.14), (3.9a), (3.9b) and (3.9c). There are also six unknown constants: the non-dimensional wavespeed c, non-dimensional wavelength L, non-dimensional fluid mass H, amplitude A from (2.10), Bernoulli constant B_1 and constant of integration C_1 from (3.13). We fix values for L, H and A, for which imposing the two mass conditions (3.10a) and (3.10b) and the amplitude constraint (2.10) yields c, B_1 and C_1 as unknowns of the problem.

https://doi.org/10.1017/jfm.2026.11966

3.5. *Numerical implementation of the steady model formulation*

We use a pseudospectral method to obtain numerical solutions to the steady system of equations described in § 3.4, in which the solutions are found by collocation. For fixed values of L, H and A, we express each solution as a Fourier series of the form

$$\{Y_{1U}, Y_{1L}, Y_{2U}\} = \sum_{m=0}^{N} \{a_m, b_m, c_m\} \cos\left(mk\hat{\xi}\right), \quad \gamma(\hat{\xi}) = \sum_{m=1}^{N} d_m \sin\left(mk\hat{\xi}\right), \tag{3.15}$$

where $k = 2\pi n/L$ as above. We use $N = 80$ and $n = 1$ throughout this work unless otherwise specified. Derivatives and integral transforms are computed spectrally by using the Fourier multipliers $d/\mathrm{d}\xi[\mathrm{e}^{imk\xi}] = imk\mathrm{e}^{imk\xi}$, $\mathscr{H}[\mathrm{e}^{imk\xi_2}] = \mathrm{i} \cdot \mathrm{sgn}(m)\mathrm{e}^{imk\xi_2}$, $\mathscr{T}[\mathrm{e}^{imk\xi_1}] = \mathrm{i} \cdot \coth(mkh)\mathrm{e}^{imk\xi_1}$ and $\mathscr{S}[\mathrm{e}^{imk\xi_1}] = \mathrm{i} \cdot \mathrm{csch}(mkh)\mathrm{e}^{imk\xi_1}$. To evaluate the solutions in physical space, we use the inverse Fourier transform with the fast-Fourier-transform algorithm.

To evaluate each matching condition (3.9*a*), (3.9*b*) and (3.9*c*), which involve functions represented by Fourier series evaluated at $\gamma(\hat{\xi})$ having the Fourier expansion from (3.15), we sum each component of the series manually. That is, when evaluating $Y_{1L}(\hat{\xi} - \gamma(\hat{\xi}))$ for instance, we calculate

$$Y_{1L}(\hat{\xi} - \gamma(\hat{\xi})) = \sum_{m=0}^{N} b_m \cos\left(mk(\hat{\xi} - \gamma(\hat{\xi}))\right) \tag{3.16}$$

term by term by resumming the series expansion. Manually resumming each term involved in the three matching conditions is the slowest part of the overall numerical scheme.

Due to the assumed symmetry of Y_{1U}, Y_{1L} and Y_{2U}, and the asymmetry of $\gamma(\hat{\xi})$, only half of the periodic domain needs to be considered. We therefore introduce the collocation points $\xi_i = -L/2 + L(i-1)/(2N+1)$ for $1 \leqslant i \leqslant N+1$, which results in $4N+6$ unknown constants obtained in total that we need to solve for. These are $\{Y_{1U}(\xi_i)\}_{i=1}^{N+1}$, $\{Y_{1L}(\xi_i)\}_{i=1}^{N+1}$, $\{Y_{2U}(\xi_i)\}_{i=1}^{N+1}$, $\{\gamma(\xi_i)\}_{i=2}^{N+1}$, c, B_1 and C_1. Next, we obtain $4N+6$ algebraic equations to close the system. Three of these constraints are given by the mass and amplitude conditions (3.10*a*), (3.10*b*) and (2.10). The remaining $4N+3$ constraints come from evaluating the remaining four equations at the collocation points: (3.14), (3.9*b*) and (3.9*c*) each provide $N+1$ constraints due to being even and (3.9*a*) provides N constraints due to being odd.

Once each of the $4N+3$ algebraic constraints have been obtained, the solution is found using Newton iteration to minimise these constraints. We continue iterating until the L^2-norm of the constraints falls below a residual of 10^{-12}, which takes approximately 3 s when $N = 100$ Fourier modes are used in (3.15). The initial guess used is either taken to be a linear solution from § 2.2, or a previously computed numerical solution obtained with specified values for L, H and A. We typically begin with the linear solution as an initial guess for a small value of A, such as $A = 10^{-5}$, and then sequentially use the computed solution as the initial guess for a larger value of A. Once the desired value has been reached, such as $A = 0.03$, we then employ arclength continuation in the (H, c) plane to explore the bifurcation curves that pass through this computed solution.

We find that significant aliasing errors emerge when computing solutions that are dominated by the vorticity interface. These are resolved by using the 36th-order Fourier filter $\exp(-36(1.2m/N)^{36})$ during the Newton-iteration procedure, and we found that best performance is obtained when only Y_{1L}, Y_{2U} and γ are de-aliased once per iteration, while no dealiasing is applied to Y_{1U}. The 36th-order filter was analysed by Hou & Li (2007) for time-dependent problems, and forms a balance between the suppression of aliasing errors

https://doi.org/10.1017/jfm.2026.11966

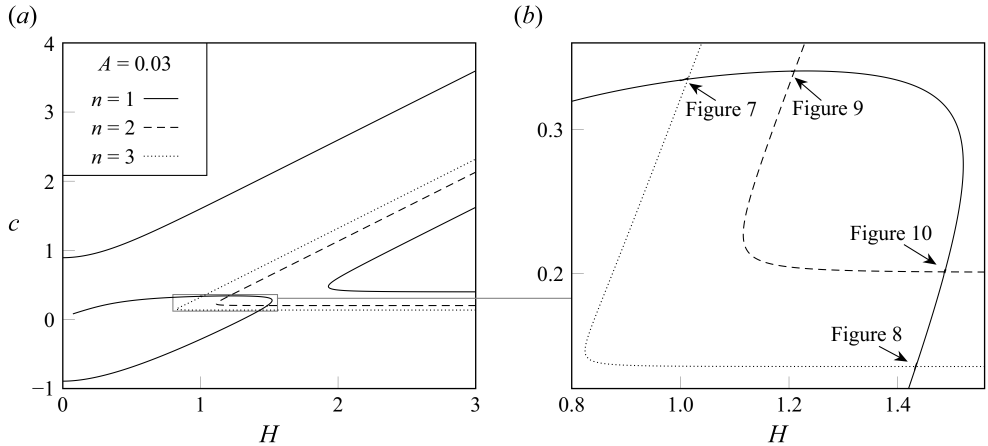

Figure 7. Branches of nonlinear solutions calculated with $A = 0.03$, $L = 5$ and $N = 80$ are shown in the (H, c) plane in panels (*a*) and (*b*). These solutions were obtained by numerical continuation using the scheme described in § 3.5. There are three distinct branches with $n = 1$ (corresponding to one wave within the periodic domain), which are analogous to the three branches of linear solutions shown in figure 4. Bifurcations arise between branches of nonlinear solutions with different wavenumbers, which are shown more clearly in (*b*). This behaviour arises due to the intersection of linear solution branches shown in figure 5.

and resolving the remaining Fourier coefficients in the spectrum. The filter used is shown below as a dashed line alongside the Fourier spectrum of each solution in figure 14 and, for the solutions in this figure that required dealiasing, we were able to compute solutions of approximately three times larger amplitude than those computed without dealiasing.

4. Finite-amplitude numerical solutions

We now compute fully nonlinear solutions of our system using the numerical scheme described in § 3.5. This boundary-integral method involves the four unknown functions $Y_{1U}(\xi_1)$, $Y_{1L}(\xi_1)$, $Y_{2U}(\xi_2)$ and $\gamma(\hat{\xi})$. When presenting results for each interface, we calculate the free surface $\zeta_1(x)$ from the parametrisation $(X_{1U}(\xi_1), Y_{1U}(\xi_1))$, and the vorticity interface $\zeta_2(x)$ from the parametrisation $(X_{1L}(\xi_1), Y_{1L}(\xi_1))$, where X_{1U} and X_{1L} are calculated by the harmonic relations (3.6). In each plot, we then display in the physical (x, y)-plane both $\zeta_1(x) - H$, which has the mean level of the upper interface removed, and $\zeta_2(x)$. The important non-dimensional parameters are the wavelength L, depth H, wavespeed c and amplitude A from (2.10). The value $L = 5$ is fixed throughout this section, and $N = 80$ Fourier coefficients are used in most results.

We first investigate how the linear solution branches and solution profiles from figure 4, computed with $A = 10^{-5}$ and $n = 1$, change as the amplitude A increases to a value of $A = 0.03$. By fixing the value of A, the wavespeed c is obtained (it depends on L, H and A). These larger-amplitude solutions were found by taking one nearly linear solution from each of the three solution branches in figure 4 and then slowly increasing A throughout consecutive Newton-iteration cycles until $A = 0.03$ was reached. Numerical continuation was then used to explore the solution branches (varying with H) associated with each of these computed solutions. The results are shown in figure 7(*a*). We will refer to each of the $n = 1$ solution branches as the upper, lower left and lower right branches. Two of the solution branches with $n = 1$ (shown with solid lines), namely the upper branch and lower right branches, are qualitatively unchanged from those obtained from the linear dispersion relation, which is anticipated due to the fact that the first weakly nonlinear

https://doi.org/10.1017/jfm.2026.11966

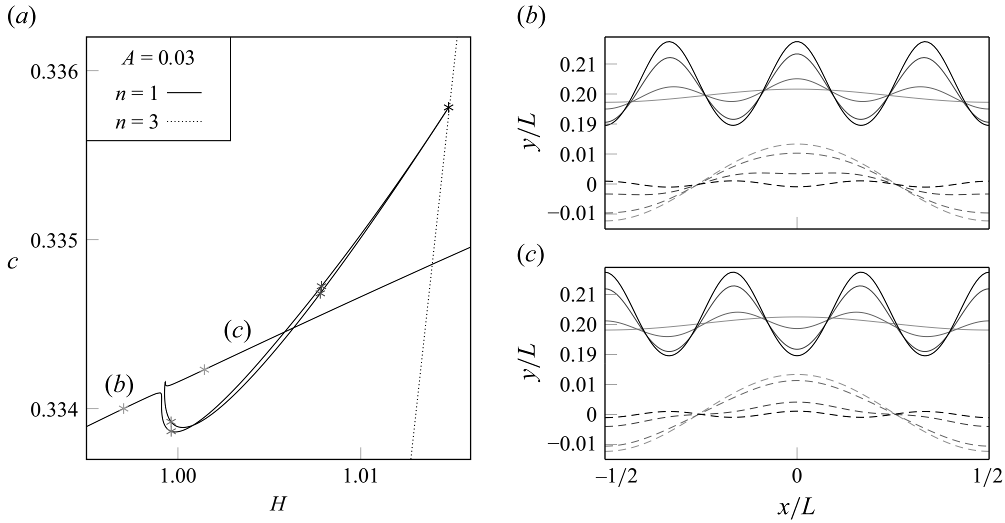

Figure 8. (a) Branches of nonlinear solutions calculated with $A = 0.03$, $L = 5$ and $N = 80$ are shown in the vicinity of the (1,3)-bifurcation point. Two $n = 1$ branches (solid) bifurcate from the same location on the $n = 3$ branch (dotted). In (b) and (c) four solution profiles are shown across each bifurcation, and the location of these in the (H, c) parameter space are shown with asterisks in (a). The free surface $\zeta_1(x)$ (solid) and vorticity interface $\zeta_2(x)$ (dashed) are shown with a broken y axis.

correction to the wavespeed vanishes (Brevik 1978). The third solution branch, in the lower left of figure 7(a), is both quantitatively and qualitatively different from the corresponding linear branch as it no longer forms one continuous curve, but rather splits up into several distinct curves that bifurcate from solutions branches with larger values of n (in fact, there are likely to be infinitely-many disjoint branches). These additional solution branches, shown dashed for $n = 2$ and dotted for $n = 3$, contain multiple wave periods within the periodic domain. For instance, solutions on the branch with $n = 3$ have Fourier modes $a_1 = 0$, $a_2 = 0$ and $a_3 \neq 0$. This behaviour was anticipated by the crossing of linear solution branches shown in figure 5; some of the corresponding bifurcations are shown in more detail in figure 7(b). Note that only the $(1, 2)$ and $(1, 3)$ bifurcations have been resolved in this figure. Note that in the absence of the shear layer ($H = 0$), there are two possible values of the wavespeed, corresponding to gravity waves of the same form travelling to the left and right. However, for $H > 0$ there are three possible values as shown in figure 7(a). The middle branch therefore forms a singular perturbative problem as $H \to 0$ and $c \to 0$. As $H \to 0$ along this branch, the crest of the internal wave broadens significantly which results in a very narrow and deep wave trough. This is the mechanism by which large-amplitude internal waves exist when the free surface is of small amplitude and the non-dimensional shear-layer depth diminishes. The resultant solution resembles a pure internal solitary wave of depression in a two-layer system (Helfrich & Melville 2006).

Nonlinear solutions were previously obtained in this model by Milinazzo & Saffman (1990). However, only one smooth solution branch was obtained in their work, which is that with the largest value of the wavespeed c from figure 7 in which the solutions are dominated by the free surface $\zeta_1(x)$. The solutions along the other branches, as well as the bifurcations between them, have not been studied previously.

Solutions close to each bifurcation point are shown in figures 8–11. In figure 8, the first $(1, 3)$ bifurcation is shown. It is the result of resonance between the shear wave mode of $n = 1$ and the gravity-wave mode $n = 3$. Here, there are two $n = 1$ bifurcation

https://doi.org/10.1017/jfm.2026.11966

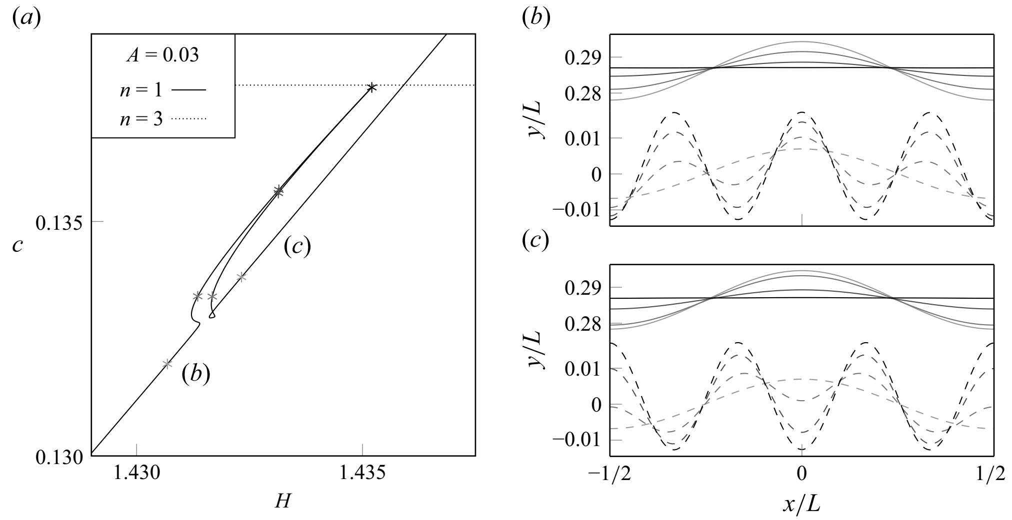

Figure 9. (a) Branches of nonlinear solutions calculated with $A = 0.03$, $L = 5$ and $N = 80$ are shown in the vicinity of the (1,3)-bifurcation point. Two $n = 1$ branches (solid) bifurcate from the same location on the $n = 3$ branch (dotted). In (b) and (c) four solution profiles are shown across each bifurcation, and the location of these in the (H, c) parameter space are shown with asterisks in (a). The free surface $\zeta_1(x)$ (solid) and vorticity interface $\zeta_2(x)$ (dashed) are shown with a broken y axis.

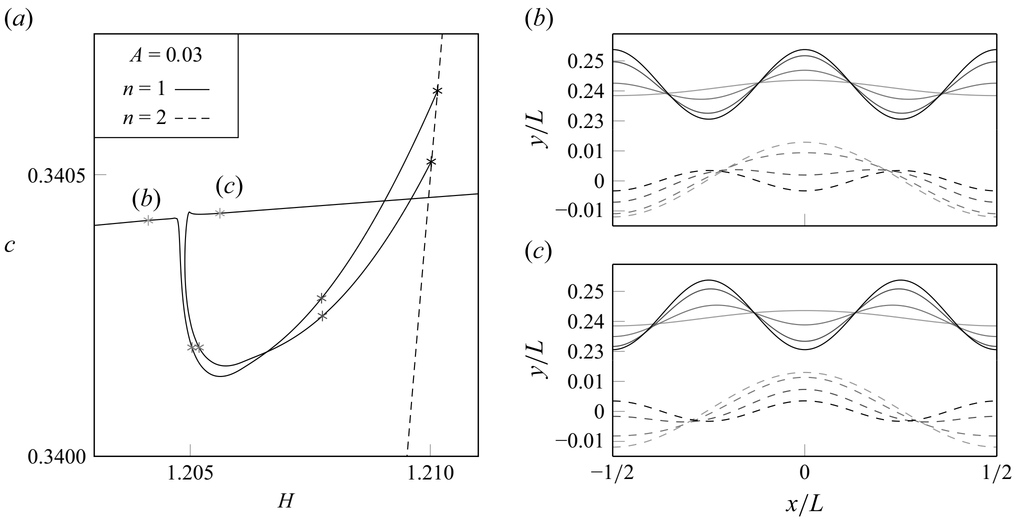

Figure 10. (a) Branches of nonlinear solutions calculated with $A = 0.03$, $L = 5$ and $N = 80$ are shown in the vicinity of the (1,2)-bifurcation point. Two $n = 1$ branches (solid) bifurcate from different locations on the $n = 2$ branch (dashed). In (b) and (c) four solution profiles are shown across each bifurcation, and the location of these in the (H, c) parameter space are shown with asterisks in (a). The free surface $\zeta_1(x)$ (solid) and vorticity interface $\zeta_2(x)$ (dashed) are shown with a broken y axis.

curves that stem from the same location on the $n = 3$ bifurcation curve. Four solutions along each of these $n = 1$ solution curves are shown in panels (b) and (c). In both cases, the $n = 1$ solutions are dominated by the vorticity interface $\zeta_2(x)$, while the transition to a solution on the $n = 3$ branch is dominated by the free surface $\zeta_1(x)$. However, while the initial solutions on the $n = 1$ solution branch are very similar and the final solutions

https://doi.org/10.1017/jfm.2026.11966

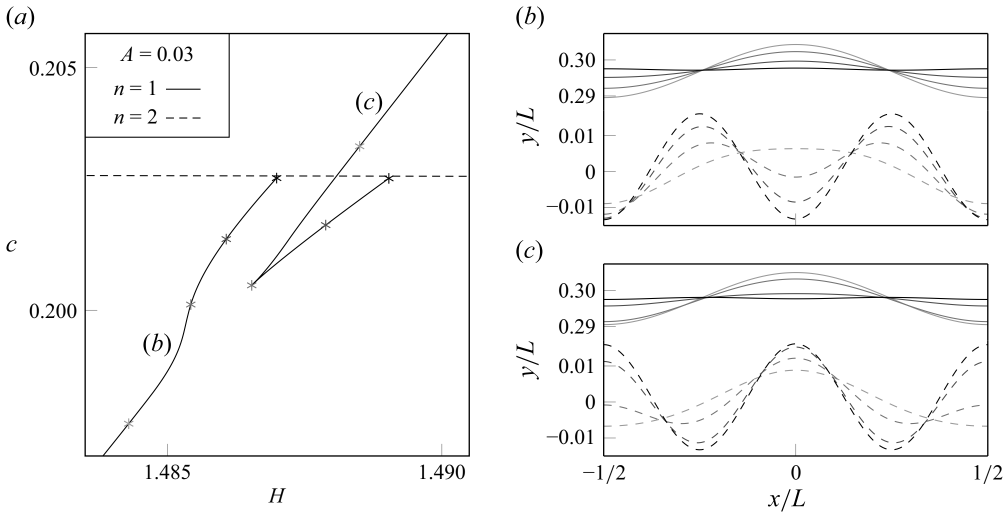

Figure 11. (*a*) Branches of nonlinear solutions calculated with $A = 0.03$, $L = 5$ and $N = 80$ in the vicinity of the (1,2)-bifurcation point. Two $n = 1$ branches (solid) bifurcate from different locations on the $n = 2$ branch (dashed). In (*b*) and (*c*) four solution profiles are shown across each bifurcation, and the location of these in the (H, c) parameter space are shown with asterisks in (*a*). The free surface $\zeta_1(x)$ (solid) and vorticity interface $\zeta_2(x)$ (dashed) are shown with a broken y axis.

on the $n = 3$ solution branch are identical, the transition between these is significantly different due to a phase shift emerging between the two $n = 3$ solutions at the bifurcation point. Similar behaviour is observed close to the second (1, 3) bifurcation point shown in figure 9. Here, two $n = 1$ branches bifurcate from the same location on the $n = 3$ branch. The key difference here is that the $n = 1$ solutions are dominated by the free surface $\zeta_1(x)$ and bifurcate from an $n = 3$ solution dominated by the vorticity interface $\zeta_2(x)$. This bifurcation is due to the resonance between the $n = 1$ gravity-wave mode and the $n = 3$ shear wave mode.

The bifurcations between solution branches with $n = 1$ and $n = 2$ are shown in figures 10 and 11. In each of these, two $n = 1$ branches bifurcate from different locations on the $n = 2$ branch. The solutions shown in figure 10 transition from $n = 1$ solutions dominated by the vorticity interface $\zeta_2(x)$ to $n = 2$ solutions dominated by the free surface $\zeta_1(x)$. Conversely, those shown in figure 11 transition from $n = 1$ solutions dominated by the free surface $\zeta_1(x)$ to $n = 2$ solutions dominated by the vorticity interface $\zeta_2(x)$. In each case, the bifurcation occurs across a very small region of parameter space and results in a major change in the solution profiles.

4.1. *Solutions of limiting amplitude*

We next investigate the behaviour of solution profiles as they transition to waves of limiting form. By taking the six solutions with $A = 0.03$ and $n = 1$ from figure 7 that have either $H = 0.5$ or $H = 2.5$, we increase the amplitude A until the decay of the Fourier coefficients plateaus. These six solutions correspond to those for $A = 10^{-5}$, denoted by (a, d, f) and (c, g, i) in figure 4, where (d, i) and (a, c, f, g) represented the shear and gravity-wave modes, respectively. The plateau of the Fourier coefficients is indicative of the clustering of a countably infinite number of singularities in the analytic continuation of the solution profiles, which results in the formation of a corner (which is also a stagnation point) at the wave crest. The specific termination criterion used here is that the largest of

https://doi.org/10.1017/jfm.2026.11966

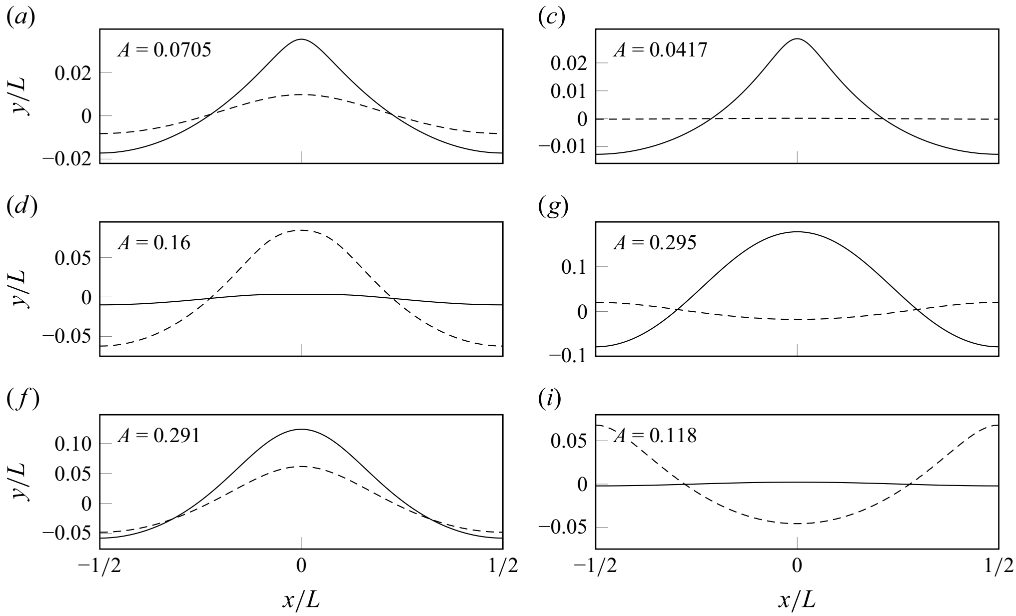

Figure 12. Nonlinear solutions of near maximum amplitude calculated with $L = 5$ and $N = 100$ Fourier coefficients are shown. The free surface $\zeta_1(x)$ (solid) and vorticity interface $\zeta_2(x)$ (dashed) are overlain. The labelling (a–i) matches with that used for the linear solutions shown in figure 4; solutions (a, d, f) have $H = 0.5$ and (c, g, i) have $H = 2.5$. To compute each solution we have increased the amplitude A until the largest of the Fourier coefficients (a_N, b_N, c_N, d_N) from (3.15) exceeds 10^{-10}. The wavespeed c, momentum P and energy E for these six solutions are given in table 1, while streamlines are shown in figure 13.

the four Fourier coefficients a_N, b_N, c_N and d_N from (3.15) exceeds 10^{-10}. In figure 12, we show six near-limiting solutions calculated with $N = 100$ Fourier modes. The labelling of these matches that used for the linear solutions in figure 4. These solutions display different transitions to solutions of maximal form. For the solutions shown in (d) and (i), the vorticity interface $\zeta_2(x)$ first becomes limiting, whereas for the solutions shown in (a), (c), (g) and (f), the free surface $\zeta_1(x)$ first becomes limiting. We observe that the amplitudes of limiting free surface and internal waves differ greatly depending on the parameter values, or wave modes. For instance, the amplitudes of $\zeta_1(x)$ in isolation for each of the six profiles is $A_1 = (0.0525, 0.0414, 0.0134, 0.257, 0.181, 0.00432)$ in alphabetical order, whereas those for $\zeta_2(x)$ are $A_2 = (0.0180, 0.000318, 0.147, 0.0381, 0.110, 0.114)$. Note that the amplitude of the limiting gravity (Stokes) wave on an irrotational fluid of infinite depth is 0.1412 (Cokelet 1977). This limiting solution forms a corner at the wave crest with an internal angle of 120 degrees. This also occurs for limiting waves with vorticity (Kozlov & Lokharu 2021).

Streamlines and stagnation points for each of the six solutions displayed in figure 12 are shown in figure 13. These were calculated using the method described in Appendix B, which finds values for the internal velocity field within each fluid layer from solutions of the boundary-integral scheme. Interestingly, closed streamlines – and therefore stagnation points – are observed within the shear layer for solutions (d, g, i). For fluids with constant vorticity, stagnation points typically emerge either within the fluid or on the free surface at the lines of symmetry $x = 0$, $x = \pm L/2$ (Ribeiro *et al.* 2017). Solution (d), which has two wave crests near $x = 0$ on the free surface $\zeta_1(x)$, has three stagnation points: one inside the

https://doi.org/10.1017/jfm.2026.11966

Solution	c	P	E	Solution	c	P	E
11(a)	1.1623	0.6685	0.9147	11(c)	3.1112	15.6526	41.8264
11(d)	0.2838	0.7757	0.9158	11(g)	0.8764	14.3236	38.5486
11(f)	−0.8090	0.0600	1.4275	11(i)	0.4261	15.7176	41.7431

Table 1. Wavespeed, momentum and energy values are recorded, to four decimal places, for the six solutions shown in both figures 12 and 14. The wavespeed c forms an unknown of the problem, while the momentum P and energy E are calculated from (3.11b) and (3.11a).

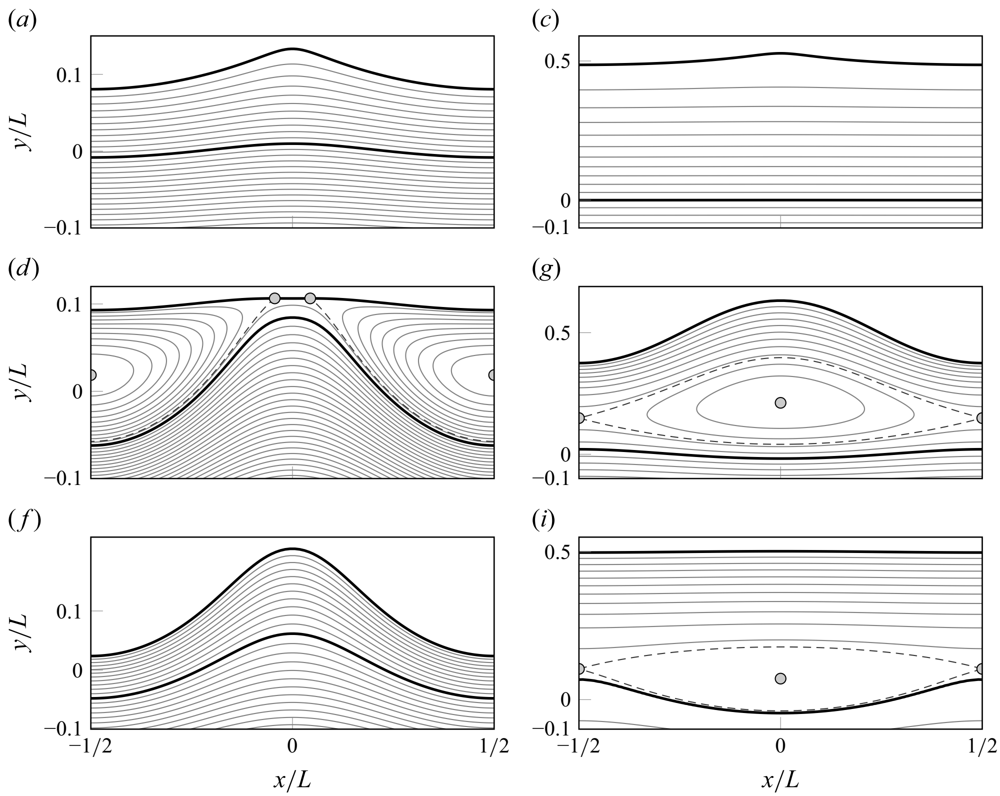

Figure 13. Streamlines and stagnation points are shown for the six solution profiles from figure 12. Streamlines (shown in grey) are calculated as contours of the streamfunctions $\hat{\psi}_1$ and $\hat{\psi}_2$ defined in (B1). Stagnation points (shown with circles) are calculated from (B2) and (B3). Ten streamlines (solid grey) are shown in the upper fluid layer for each profile, with the value on each contour uniformly dividing the range $\min(\hat{\psi}_1)$ to $\max(\hat{\psi}_1)$. The same spacing, $[\max(\hat{\psi}_1) - \min(\hat{\psi}_1)]/11$, between contour values has been used to plot streamlines in the lower fluid layer. Additional streamlines (dashed grey) show those emerging from stagnation points.

fluid and two on the free surface. Solutions (g) and (i) each have two internal stagnation points, one at $x = 0$ and another at $x = \pm L/2$.

The Fourier spectrum for each of the six solutions plotted in figure 12 is displayed in figure 14. The decay of these Fourier coefficients indicates which of the two interfaces first develops a corner at the wavecrest as the amplitude continues to increase. For solutions (d) and (i), it is the vorticity interface $\zeta_2(x)$ that has the slowest decay of Fourier coefficients, which indicates that this interface will become limiting first.

https://doi.org/10.1017/jfm.2026.11966

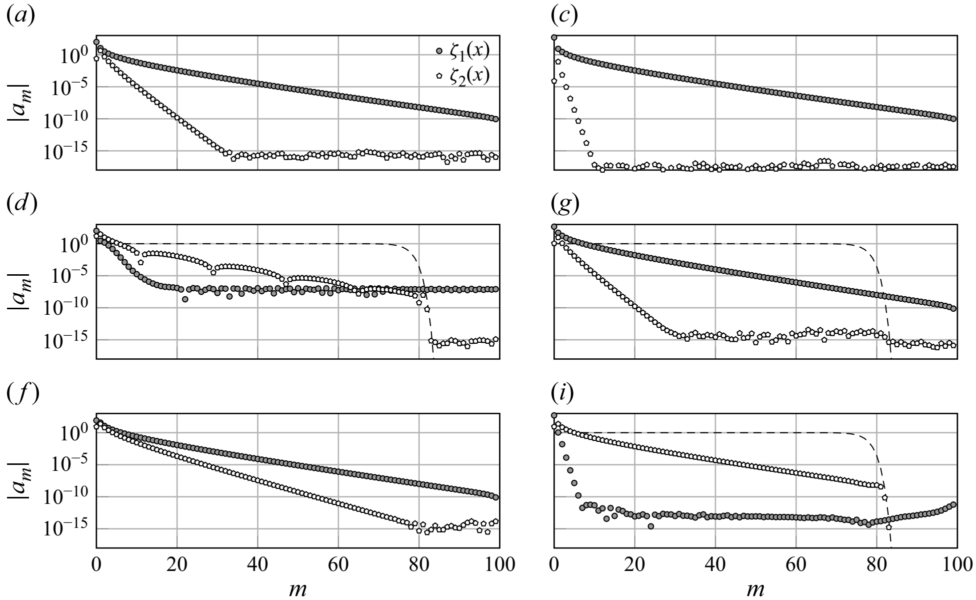

Figure 14. The Fourier spectrum for each of the six solutions from figure 12 is shown. The absolute value of each Fourier coefficient for the free surface $\zeta_1(x)$, corresponding to a_m from (3.15), is shown with filled circles and that for the vorticity interface $\zeta_2(x)$, corresponding to c_m from (3.15), is shown with hollow pentagons. The Fourier filter $\exp\left(-36(1.2m/N)^{36}\right)$, used for solutions with a slow decay of b_m, is shown dashed in (*d*) and (*i*).

5. Conclusion and discussion

We have computed new solutions for travelling waves that propagate under the combined effects of constant background vorticity (confined within a shear layer) and gravity. To describe the motions of the two free boundaries, which are the top and bottom surfaces of the shear layer, we have adopted a boundary-integral formulation via conformal mapping and have used a pseudospectral method to find its numerical solutions. The primary advantage of this methodology is the straightforward generalisation of the steady formulation to study the time-dependent dynamics of nonlinear waves.

The solution branches we have calculated contain solutions with qualitatively different features depending on two physical parameters, the non-dimensional wavelength L and the non-dimensional shear-layer thickness H. In general, for the shear mode, the vorticity interface displacement ζ_2 is much greater than the free-surface displacement ζ_1. For the gravity mode, ζ_2 is comparable to or smaller than ζ_1 depending on H. It is also observed that both interfaces have the same polarity (with wave crests at the same value of x) before the basic flow loses its stability due to the collision of the shear and gravity modes, while they have opposite polarities (with a crest and a trough at the same value of x) above a specific value of H after the basic flow becomes restabilised. In addition, resonances between the shear and gravity modes can occur when the wavelength L of one mode is an integer multiple of the other. Then, the transition between non-resonant and resonant solutions appears over a very small region of parameter space. We have shown such transitions in detail for the (1, 2) and (1, 3) bifurcations, where the ratios between the two wavelengths are 2 and 3, respectively.

While these resonances are not possible for gravity waves without a shear layer, it has been known that the bifurcations of nonlinear solutions found in the present study

https://doi.org/10.1017/jfm.2026.11966

emerge in many other surface wave models. For instance, in the study of gravity-capillary waves, a countably infinite number of solution branches emerge in the singular perturbative limit of small surface tension corresponding to a general $(1, n)$ bifurcation (Champneys *et al.* 2002), and these solutions contain visible oscillatory ripples with an exponentially small amplitude (Shelton *et al.* 2021). The fully nonlinear resonance conditions were derived by Shelton & Trinh (2022) by studying Stokes phenomenon in the limit of small surface tension. The general $(1, n)$ bifurcations in the present study emerge in the limit of $H \to 0$, which corresponds to a small dimensional shear-layer thickness. However, no such oscillatory behaviour was observed in either the solution profiles or the Fourier spectrum associated with exponentially small components of a parametric transseries (Shelton & Trinh 2022).

While we have partially developed the time-dependent mapping for the two-layer system in § 3, the full derivation of the time-evolution conformal equations remains a topic for future work, where it is needed to derive the time-evolution equations for the elevation and velocity potential on each interface, Y_{1U}, Y_{1L}, Φ_{1U} and Φ_{1L}. This would allow for the study of the linear stability of the nonlinear travelling-wave solutions with respect to small-amplitude perturbations, as well as the general evolution of a perturbed shear layer, e.g. by surface wind forcing. The stability of nonlinear travelling-wave solutions in finite-depth water of constant vorticity was studied by Francius & Kharif (2017) who found that shear both suppresses the long-wave instability and enhances resonance-based instabilities. It would be of interest to find the stability characteristics of the new solutions computed here with a vorticity jump.

The vorticity layer studied in this work, motivated by the effect of horizontal shear induced by wind, can also emerge in other geophysical flows. For example, in density-stratified oceans with thin pycnoclines often represented by layered models (Helfrich & Melville 2006), large-amplitude internal gravity waves travelling on the interfaces have been frequently observed in field and laboratory experiments (Grue *et al.* 1999; Ramp *et al.* 2004; Kodaira *et al.* 2016). Nevertheless, the internal gravity waves suffer locally near the maximum displacement from the wave-induced Kelvin–Helmholtz instability (Jo & Choi 2002; Carr *et al.* 2008) and thin vorticity layers are then induced at the interfaces by turbulent mixing resulting from the instability (Dimotakis 2005). Under this situation, it would be of interest to extend the current formulation to investigate the effects of thin vorticity layers on large-amplitude internal gravity waves at the interface between two layers of different density.

Acknowledgements. We thank each of the anonymous reviewers for their comments that have improved the clarity of our paper.

Funding. The work of W.C. was supported by the US National Science Foundation through grant number DMS-2108524.

Declaration of interests. The authors report no conflict of interest.

Appendix A. The boundary-value problem in dimensional variables

Consider two incompressible and immiscible fluids with equal densities. Assume that the flow is two-dimensional, with x the horizontal coordinate and y the vertical one. The first fluid, confined in the range $-\infty < y \leqslant \zeta_2(x, t)$, is assumed to be irrotational. The second, lying above the first and located in the range $\zeta_2(x, t) \leqslant y \leqslant \zeta_1(x, t)$, has constant vorticity, $-\omega$. Here, $y = \zeta_1$ is the free surface, the upper boundary of the entire fluid domain. Each fluid satisfies the Euler equations within the respective domain, as well as kinematic and dynamic boundary conditions at the interfaces. We define $\boldsymbol{u}_1 = (u_1, v_1)$ and p_1 as the

https://doi.org/10.1017/jfm.2026.11966

velocity and pressure fields in the rotational fluid, and $\boldsymbol{u}_2 = (u_2, v_2)$ and p_2 as those in the irrotational fluid. Each of these quantities depends on the domain, (x, y), and on time, t.

The governing boundary-value problem then consists of the partial differential equations

$$\nabla \cdot \boldsymbol{u}_1 = 0, \qquad \frac{\partial \boldsymbol{u}_1}{\partial t} + (\boldsymbol{u}_1 \cdot \nabla)\boldsymbol{u}_1 = -\frac{1}{\rho}\nabla p_1 - g\nabla y \quad \text{for} \quad \zeta_2(x, t) \leqslant y \leqslant \zeta_1(x, t), \tag{A1a,b}$$

$$\nabla \cdot \boldsymbol{u}_2 = 0, \qquad \frac{\partial \boldsymbol{u}_2}{\partial t} + (\boldsymbol{u}_2 \cdot \nabla)\boldsymbol{u}_2 = -\frac{1}{\rho}\nabla p_2 - g\nabla y \quad \text{for} \quad -\infty < y \leqslant \zeta_2(x, t), \tag{A1c,d}$$

the kinematic and dynamic boundary conditions at the free surface

$$\partial_t \zeta_1 = \boldsymbol{u}_1 \cdot \nabla(y - \zeta_1) \quad \text{and} \quad p_1 = 0 \quad \text{at } y = \zeta_1(x, t), \tag{A1e,f}$$

the kinematic condition and continuity of velocity at the vorticity interface

$$\partial_t \zeta_2 = \boldsymbol{u}_2 \cdot \nabla(y - \zeta_2) \quad \text{and} \quad \boldsymbol{u}_1 = \boldsymbol{u}_2 \quad \text{at } y = \zeta_2(x, t), \tag{A1g,h}$$

as well as a decay condition on the irrotational velocity field

$$(u_2, v_2) \to (0, 0) \quad \text{as} \quad y \to -\infty. \tag{A1i}$$

In (A1b,d), ρ is the fluid density and g is the constant value of gravitational acceleration. Note that continuity of pressure at the vorticity interface, $p_1 = p_2$ at $y = \zeta_2(x, t)$, follows directly from enforcing continuity of velocity in (A1h).

A.1. *Potential-flow boundary-value problem*

We now simplify the boundary-value problem for the Euler equations presented in (A1a–i). Using a Helmholtz decomposition to write each velocity field as the sum of the gradient of a potential function and the curl of a solenoidal vector, we obtain

$$\boldsymbol{u}_1 = \nabla\phi_1 + (\omega y, 0) \quad \text{and} \quad \boldsymbol{u}_2 = \nabla\phi_2. \tag{A2a,b}$$

Thus, the vorticity of the fluid in the shear layer is equal to $-\omega$, while that in the irrotational fluid is zero.

First, we evaluate the continuity equations (A1a,c), which yields Laplace's equation for the potential in each fluid domain

$$\nabla^2\phi_1 = 0 \quad \text{for} \quad \zeta_2(x, t) \leqslant y \leqslant \zeta_1(x, t), \tag{A3a}$$

$$\nabla^2\phi_2 = 0 \quad \text{for} \quad -\infty < y \leqslant \zeta_2(x, t). \tag{A3b}$$

Next, we may integrate the Euler equations (A1b) in the vortical fluid layer. Since $\partial_t \boldsymbol{u}_1 = \nabla(\partial_t\phi_1)$ and $(\boldsymbol{u}_1 \cdot \nabla)\boldsymbol{u}_1 = \nabla(\boldsymbol{u}_1 \cdot \boldsymbol{u}_1)/2 - \nabla(\omega\psi_1 + \omega^2 y^2/2)$, we may integrate to obtain Bernoulli's equation in each fluid. Note that we have introduced ψ_1, which is the harmonic conjugate of ϕ_1. Evaluating the Bernoulli equation at the free surface and invoking conditions (A1a) yields the dynamic boundary condition

$$\phi_{1t} + \frac{1}{2}(\phi_{1x}^2 + \phi_{1y}^2) + (\omega y - c)\phi_{1x} - \omega\psi_1 + gy = B_1 \tag{A3c}$$

at the free surface $y = \zeta_1(x, t)$. Continuity of the velocity field then requires

$$\phi_{1x} + \omega y = \phi_{2x} \quad \text{and} \quad \phi_{1y} = \phi_{2y} \tag{A3d}$$

https://doi.org/10.1017/jfm.2026.11966

at the vorticity interface $y = \zeta_2(x, t)$. To obtain the kinematic boundary conditions, we substitute the velocity field decompositions (A2*a*,*b*) into conditions (A1*e*,*g*) yielding

$$\zeta_{1t} = \phi_{1y} - \zeta_{1x}(\phi_{1x} + \omega y - c) \quad \text{at} \quad y = \zeta_1(x, t), \tag{A3e}$$

$$\left.\begin{array}{l} \zeta_{2t} = \phi_{2y} - \zeta_{2x}(\phi_{2x} - c) \\ \zeta_{2t} = \phi_{1y} - \zeta_{2x}(\phi_{1x} + \omega y - c) \end{array}\right\} \quad \text{at} \quad y = \zeta_2(x, t). \tag{A3f}$$

Lastly, we have the decay conditions $(\phi_{2x}, \phi_{2y}) \to (0, 0)$ as $y \to -\infty$. By applying the Cauchy–Riemann equations to the analytic function $\phi_2 + \mathrm{i}\psi_2$, these may be integrated to obtain

$$(\phi_2, \psi_2) \to (0, 0) \quad \text{as} \quad y \to -\infty. \tag{A3g}$$

The constants of integration have been set to zero, which removes the invariance of ϕ_2 and ψ_2 with respect to additive constants.

Note further that ψ_1 and ψ_2, the harmonic conjugates of each velocity potential, are continuous across the vorticity interface so that

$$\psi_2 = \psi_1 + \omega y^2/2 \quad \text{at} \quad y = \zeta_2(x, t). \tag{A4}$$

A.2. *Conserved quantities*

Our model formulation has four conserved quantities. These are the mass of each of the two fluid layers separately, the horizontal momentum and the total energy.

A.2.1. *Mass*

Conservation of mass yields the conditions

$$h = \frac{1}{\lambda}\int_{-\lambda/2}^{\lambda/2} \zeta_1(x, t)\,\mathrm{d}x, \quad 0 = \int_{-\lambda/2}^{\lambda/2} \zeta_2(x, t)\,\mathrm{d}x. \tag{A5a,b}$$

Note that (A5*a*) has dimensions of length, and (A5*b*) has dimensions of area. In (A5*b*), h represents the average depth of the shear layer over one wave period.

A.2.2. *Momentum*

The horizontal momentum is defined as the integral of the horizontal velocity, u, over the fluid domain. This yields

$$P = \int_{-\lambda/2}^{\lambda/2}\int_{-\infty}^{\zeta_2(x,t)} \phi_{2x}\,\mathrm{d}y\mathrm{d}x + \int_{-\lambda/2}^{\lambda/2}\int_{\zeta_2(x,t)}^{\zeta_1(x,t)} (\phi_{1x} + \omega y)\,\mathrm{d}y\mathrm{d}x. \tag{A6}$$

Using Green's identity to convert each integral above into an integral over each interface produces

$$P = \int_{-\lambda/2}^{\lambda/2} \left[\zeta_2\big(\phi_{2x} - \phi_{1x} + \zeta_{2x}[\phi_{2y} - \phi_{1y}]\big)\big|_{y=\zeta_2} + \zeta_1(\phi_{1x} + \zeta_{1x}\phi_{1y})\big|_{y=\zeta_1} + \frac{\omega}{2}\big(\zeta_1^2 - \zeta_2^2\big) \right]\mathrm{d}x. \tag{A7}$$

Since the velocity field is continuous across the vorticity interface $y = \zeta_2$, we have $\phi_{2y} = \phi_{1y}$ and $\phi_{2x} = \phi_{1x} + \omega y$ from (A3*d*), which simplifies the momentum expression to

$$P = \int_{-\lambda/2}^{\lambda/2} \left[\zeta_1(\phi_{1x} + \zeta_{1x}\phi_{1y})\big|_{y=\zeta_1} + \frac{\omega}{2}\big(\zeta_1^2 + \zeta_2^2\big) \right]\mathrm{d}x. \tag{A8}$$

https://doi.org/10.1017/jfm.2026.11966

A.2.3. *Energy*
The energy is the sum of kinetic and gravitational potential energies

$$E = \int_{-\lambda/2}^{\lambda/2} \int_{-\infty}^{\zeta_1(x,t)} \left(u^2 + v^2\right) \mathrm{d}y\mathrm{d}x + g \int_{-\lambda/2}^{\lambda/2} \int_{-\infty}^{\zeta_1(x,t)} y \, \mathrm{d}y\mathrm{d}x. \tag{A9}$$

By substituting for the decompositions of u and v in each fluid domain from (A2), we obtain

$$E = \int_{-\lambda/2}^{\lambda/2} \int_{-\infty}^{\zeta_2} \left(\phi_{2x}^2 + \phi_{2y}^2\right) \mathrm{d}y\mathrm{d}x + \int_{-\lambda/2}^{\lambda/2} \int_{\zeta_2}^{\zeta_1} \left(\phi_{1x}^2 + \phi_{1y}^2 + 2\omega y \phi_{1x} + \omega^2 y^2\right) \mathrm{d}y\mathrm{d}x + \frac{g}{2} \int_{-\lambda/2}^{\lambda/2} \zeta_1^2 \, \mathrm{d}x. \tag{A10}$$

Through application of Green's theorem to (A10), a reduction can be made to obtain an integral involving quantities evaluated only on the free surface $y = \zeta_1$ and vorticity interface $y = \zeta_2$. This yields

$$E = \int_{-\lambda/2}^{\lambda/2} \Bigg(\left[\phi_2(\phi_{2y} - \zeta_{2x}\phi_{2x}) - \phi_1(\phi_{1y} - \zeta_{2x}\phi_{1x}) - \omega y^2(\phi_{1x} + \zeta_{2x}\phi_{1y})\right]_{y=\zeta_2} + \left[\phi_1(\phi_{1y} - \zeta_{1x}\phi_{1x}) + \omega y^2(\phi_{1x} + \zeta_{1x}\phi_{1y})\right]_{y=\zeta_1} + \frac{\omega^2}{3}\left(\zeta_1^3 - \zeta_2^3\right) + \frac{g}{2}\zeta_1^2 \Bigg) \mathrm{d}x. \tag{A11}$$

Appendix B. Streamlines and stagnation points

In the frame of reference moving with the travelling wave, streamlines are defined as level sets of the streamfunctions

$$\hat{\psi}_1(x_1, y_1) = \psi_1(x_1, y_1) + \frac{1}{2} y_1^2 - c y_1, \quad \hat{\psi}_2(x_2, y_2) = \psi_2(x_2, y_2) - c y_2, \tag{B1}$$

for $\zeta_2(x) \leqslant y_1 \leqslant \zeta_1(x)$ and $-\infty < y_2 \leqslant \zeta_2(x)$, respectively. Note that the functions ψ_1 and ψ_2 were defined as the harmonic conjugate of the velocity potential and so are not streamfunctions. Stagnation points, at which the velocity field is zero, may either be considered as minima or maxima of the streamfunctions from (B1), or equivalently as solutions to

$$\partial_{x_1} \hat{\psi}_1 \equiv -\psi_{1x} = 0, \quad \partial_{y_1} \hat{\psi}_1 \equiv \psi_{1y} + y_1 - c = 0, \tag{B2}$$

for $\zeta_2(x) \leqslant y_1 \leqslant \zeta_1(x)$, and

$$\partial_{x_2} \hat{\psi}_2 \equiv -\psi_{2x} = 0, \quad \partial_{y_2} \hat{\psi}_2 \equiv \psi_{2y} - c = 0, \tag{B3}$$

for $-\infty < y_2 \leqslant \zeta_2(x)$.

The boundary-integral formulation developed in § 3 by conformal mapping yields the solutions Y_{1U}, Y_{1L}, Y_{2U}. These were defined in (3.3) as $Y_{1U}(\xi_1) = y_1(\xi_1, h)$, $Y_{1L}(\xi_1) = y_1(\xi_1, 0)$ and $Y_{2U}(\xi_2) = y_2(\xi_2, 0)$, where the time dependence of each solution has been omitted. We now describe how to compute the internal velocity field as required to study streamlines and stagnation points of the solutions. To evaluate the streamfunctions (B1), we require values for $\psi_1(\xi_1, \eta_1)$, $y_1(\xi_1, \eta_1)$, $\psi_2(\xi_2, \eta_2)$ and $y_2(\xi_2, \eta_2)$. Then, to map these back to the physical domain we also require values for $x_1(\xi_1, \eta_1)$ and $x_2(\xi_2, \eta_2)$.

Starting with the lower fluid layer in the range $-\infty < y_2 \leqslant \zeta_2(x)$, or equivalently in conformal space in the range $-\infty < \eta_2 \leqslant 0$, we take the solution $Y_{2U}(\xi_2)$ and calculate

https://doi.org/10.1017/jfm.2026.11966

$\Psi_{2U}(\xi_2)$ by (3.13). Then, by the series solutions (3.1*a*) and (3.1*b*) we calculate values within the fluid spectrally by the Fourier multiplier relations

$$x_2(\xi_2, \eta_2) = \xi_2 - \mathscr{F}^{-1}\left[\mathrm{i} \cdot \mathrm{sgn}(m)\mathrm{e}^{|m|k\eta_2}\mathscr{F}\left[Y_{2U}\right]\right], \tag{B4a}$$

$$y_2(\xi_2, \eta_2) = \eta_2 + \mathscr{F}^{-1}\left[\mathrm{e}^{|m|k\eta_2}\mathscr{F}\left[Y_{2U}\right]\right], \tag{B4b}$$

$$\psi_2(\xi_2, \eta_2) = \mathscr{F}^{-1}\left[\mathrm{e}^{|m|k\eta_2}\mathscr{F}\left[\Psi_{2U}\right]\right], \tag{B4c}$$

where $k = 2\pi/L$ and $\mathscr{F}$ denotes the Fourier transform. Next, for the upper fluid layer we begin with solutions for $Y_{1U}(\xi_1)$ and $Y_{1L}(\xi_1)$ and calculate $\Psi_{1L}(\xi_1)$ and $\Psi_{1L}(\xi_1)$ from (3.13). Then, from the series solutions (3.2*a*) and (3.2*b*), we have that

$$x_1(\xi_1, \eta_1) = \xi_1 + \mathscr{F}^{-1}\left[\alpha\mathscr{F}\left[Y_{1U}\right] + \beta\mathscr{F}\left[Y_{1L}\right]\right], \tag{B5a}$$

$$y_1(\xi_1, \eta_1) = \eta_1 + \overline{Y_{1L}} + \mathscr{F}^{-1}\left[\gamma\mathscr{F}\left[Y_{1U}\right] + \delta\mathscr{F}\left[Y_{1L}\right]\right], \tag{B5b}$$

$$\psi_1(\xi_1, \eta_1) = \frac{\left(\overline{\Psi_{1U}} - \overline{\Psi_{1L}}\right)}{h}\eta_1 + \overline{\Psi_{1L}} + \mathscr{F}^{-1}\left[\gamma\mathscr{F}\left[\Psi_{1U}\right] + \delta\mathscr{F}\left[\Psi_{1L}\right]\right]. \tag{B5c}$$

Here, we have defined the average value of the function by

$$\left\{\overline{Y_{1L}}, \overline{\Psi_{1U}}, \overline{\Psi_{1L}}\right\} = \frac{1}{L}\int_{-L/2}^{L/2}\left\{Y_{1L}, \Psi_{1U}, \Psi_{1L}\right\}\mathrm{d}\xi_1, \tag{B6}$$

and also the introduce the four Fourier multipliers that take values

$$\left.\begin{aligned} \alpha = -\mathrm{i}\frac{\mathrm{e}^{mk\eta_1} + \mathrm{e}^{-mk\eta_1}}{\mathrm{e}^{mkh} - \mathrm{e}^{-mkh}}, \quad \beta = \mathrm{i}\frac{\mathrm{e}^{mk(h-\eta_1)} + \mathrm{e}^{-mk(h-\eta_1)}}{\mathrm{e}^{mkh} - \mathrm{e}^{-mkh}}, \\ \gamma = \frac{\mathrm{e}^{mk\eta_1} - \mathrm{e}^{-mk\eta_1}}{\mathrm{e}^{mkh} - \mathrm{e}^{-mkh}}, \quad \delta = \frac{\mathrm{e}^{mk(h-\eta_1)} - \mathrm{e}^{-mk(h-\eta_1)}}{\mathrm{e}^{mkh} - \mathrm{e}^{-mkh}}, \end{aligned}\right\} \tag{B7}$$

for $m \neq 0$, and $(\alpha, \beta, \gamma, \delta) = (0, 0, 0, 0)$ for $m = 0$. It is easily verified that when evaluating each of the relations (B5) at either $\eta_1 = 0$ or $\eta_1 = h$ the expression reduces down to yield the respective boundary-integral solution.

When calculating streamlines, as in figure 13 for example, we have evaluated each function within the fluid at 500 values of η_1 between 0 and h, and at 200 values of η_2 between 0 and -1.

References

Banner, M.L. & Phillips, O.M. 1974 On the incipient breaking of small scale waves. *J. Fluid Mech.* **65** (4), 647–656.

Blyth, M.G. & Părău, E.I. 2016 The stability of capillary waves on fluid sheets. *J. Fluid Mech.* **806**, 5–34.

Brevik, I. 1978 Higher-order waves propagating on constant vorticity currents in deep water. *Coast. Engng* **2**, 237–259.

Caponp, E.A., Yuen, H.C., Milinazzo, F.A. & Saffman, P.G. 1991 Water-wave instability induced by a drift layer. *J. Fluid Mech.* **222**, 207–213.

Carr, M., Fructus, D., Grue, J., Jensen, A. & Davies, P.A. 2008 Convectively induced shear instability in large amplitude internal solitary waves. *Phys. Fluids* **20** (12), 126601.

Champneys, A.R., Vanden-Broeck, J.-M. & Lord, G.J. 2002 Do true elevation gravity–capillary solitary waves exist? A numerical investigation. *J. Fluid Mech.* **454**, 403–417.

Chen, B. & Saffman, P.G. 1979 Steady gravity-capillary waves on deep water—I. Weakly nonlinear waves. *Stud. Appl. Maths* **60** (3), 183–210.

Chen, B. & Saffman, P.G. 1980 Steady gravity-capillary waves on deep water—II. Numerical results for finite amplitude. *Stud. Appl. Maths* **62** (2), 95–111.

https://doi.org/10.1017/jfm.2026.11966

CHOI, W. 2009 Nonlinear surface waves interacting with a linear shear current. *Maths Comput. Simul.* **80** (1), 29–36.
CHOI, W. & CAMASSA, R. 1999 Exact evolution equations for surface waves. *J. Engng Mech.* **125** (7), 756–760.
COKELET, E.D. 1977 Steep gravity waves in water of arbitrary uniform depth. *Phil. Trans. R. Soc. Lond. A* **286**, 183–230, 1335.
DIMOTAKIS, P.E. 2005 Turbulent mixing. *Annu. Rev. Fluid Mech.* **37** (1), 329–356.
DYACHENKO, A.L., ZAKHAROV, V.E. & KUZNETSOV, E.A. 1996 Analytical description of the free surface dynamics of an ideal fluid (canonical formalism and conformal mapping). *Phys. Lett. A* **221**, 73–79.
FRANCIUS, M. & KHARIF, C. 2017 Two-dimensional stability of finite-amplitude gravity waves on water of finite depth with constant vorticity. *J. Fluid Mech.* **830**, 631–659.
GRUE, J., JENSEN, A., RUSÅS, P.-O. & SVEEN, J.K. 1999 Properties of large-amplitude internal waves. *J. Fluid Mech.* **380**, 257–278.
HELFRICH, K.R. & MELVILLE, W.K. 2006 Long nonlinear internal waves. *Annu. Rev. Fluid Mech.* **38** (1), 395–425.
HOU, T.Y. & LI, R. 2007 Computing nearly singular solutions using pseudo-spectral methods. *J. Comput. Phys.* **226** (1), 379–397.
JO, T. & CHOI, W. 2002 Dynamics of strongly nonlinear internal solitary waves in shallow water. *Stud. Appl. Maths* **109**, 205–228.
KODAIRA, T., WASEDA, T., MIYATA, M. & CHOI, W. 2016 Internal solitary waves in a two-fluid system with a free surface. *J. Fluid Mech.* **804**, 201–223.
KOZLOV, V.A. & LOKHARU, E.E. 2021 On rotational waves of limit amplitude. *Funct. Anal. Applics* **55** (2), 165–169.
MILES, J.W. 1957 On the generation of surface waves by shear flows. *J. Fluid Mech.* **3** (2), 185–204.
MILINAZZO, F.A. & SAFFMAN, P.G. 1990 Effect of a surface shear layer on gravity and gravity–capillary waves of permanent form. *J. Fluid Mech.* **216**, 93–101.
MURASHIGE, S. & CHOI, W. 2020 Stability analysis of deep-water waves on a linear shear current using unsteady conformal mapping. *J. Fluid Mech.* **885**, A41.
MURASHIGE, S. & CHOI, W. 2022 Two-dimensional stability analysis of finite-amplitude interfacial gravity waves in a two-layer fluid. *J. Fluid Mech.* **938**, A13.
RAMP, S.R., TANG, D., DUDA, T.F., LYNCH, J.F., LIU, A.K., CHIU, C.S., BAHR, F., KIM, H.R. & YANG, Y.J. 2004 Internal solitons in the northeastern south china sea. Part I: sources and deep water propagation. *IEEE J. Ocean Engng* **29**, 1157–1181.
RAYLEIGH, L. 1894 *The Theory of Sound*, 2nd edn. Macmillan.
RIBEIRO, R., MILEWSKI, P.A. & NACHBIN, A. 2017 Flow structure beneath rotational water waves with stagnation points. *J. Fluid Mech.* **812**, 792–814.
SAFFMAN, P.G. & YUEN, H.C. 1982 Finite-amplitude interfacial waves in the presence of a current. *J. Fluid Mech.* **123**, 459–476.
SHELTON, J., MILEWSKI, P. & TRINH, P.H. 2021 On the structure of steady parasitic gravity-capillary waves in the small surface tension limit. *J. Fluid Mech.* **922**, A16.
SHELTON, J. & TRINH, P.H. 2022 Exponential asymptotics for steady parasitic capillary ripples on steep gravity waves. *J. Fluid Mech.* **939**, A17.
STERN, M.E. & ADAM, Y.A. 1973 Capillary waves generated by a shear current in water. *Mem. Soc. R. Sci. Liege* **6** (6), 179.
SULLIVAN, P.P. & MCWILLIAMS, J.C. 2010 Dynamics of winds and currents coupled to surface waves. *Annu. Rev. Fluid Mech.* **42** (1), 19–42.
WILTON, J.R. 1915 On ripples. *Phil. Mag. Ser.* **29** (173), 688–700.

https://doi.org/10.1017/jfm.2026.11966